

MODELING MHD ACCRETION–EJECTION—FROM THE LAUNCHING AREA TO PROPAGATION SCALES

DENISS STEPANOV AND CHRISTIAN FENDT

Max Planck Institute for Astronomy, Königstuhl 17, D-69117 Heidelberg, Germany; deniss@stepanovs.org, fendt@mpia.de

Received 2014 February 19; accepted 2014 July 22; published 2014 September 2

ABSTRACT

We present the results of axisymmetric magnetohydrodynamic simulations investigating the launching of jets and outflows from a magnetically diffusive accretion disk. The time evolution of the disk structure is self-consistently taken into account. In contrast to previous works, we have applied spherical coordinates for the numerical grid, implying substantial benefits concerning the numerical resolution and the stability of the simulation. Due to the new setup, we were able to run simulations for more than 150,000 dynamical times on a domain extending 1500 inner disk radii with a resolution of up to 24 cells per disk height in the inner disk. Depending on the disk magnetization, jet launching occurs in two different but complementary regimes—jets driven predominantly by centrifugal or magnetic forces. These regimes differ in the ejection efficiency concerning mass, energy, and angular momentum. We show that it is the actual disk magnetization and not so much the initial magnetization that best describes the disk–jet evolution. Considering the actual disk magnetization, we also find that simulations starting with different initial magnetization evolve in a similar—typical—way, due to advection and diffusion, as the magnetic flux in the disk evolves in time. Exploring a new, modified diffusivity model, we confirm the self-similar structure of the global jet-launching disk, obtaining power laws for the radial profiles of the disk physical variables such as density, magnetic field strength, or accretion velocity.

Key words: accretion, accretion disks – galaxies: jets – ISM: jets and outflows – magnetohydrodynamics (MHD) – stars: mass-loss – stars: pre-main sequence

Online-only material: color figures

1. INTRODUCTION

Astrophysical jets as highly collimated beams of high-velocity material and outflows of a smaller degree of collimation and a lower speed are a ubiquitous phenomenon in a variety of astrophysical sources. The role of magnetic fields in the realm of jets and accretion disks cannot be underestimated. It is crucial for the launching, acceleration, and collimation of jets (see, e.g., Blandford & Payne 1982; Pudritz & Norman 1983; Uchida & Shibata 1985; Camenzind 1990; Pelletier & Pudritz 1992; Sauty & Tsinganos 1994; Ustyugova et al. 1995; Fendt & Camenzind 1996; Ouyed & Pudritz 1997; Pudritz et al. 2007; Fendt 2009). However, due to the complexity of the physical problem, the exact time evolution and geometry of these processes is still under debate.

Jets and outflows from young stellar objects (YSOs) and active galactic nuclei (AGNs) clearly affect their environment, and, thus, at the same time the formation process of the objects that are launching them (see, e.g., Banerjee et al. 2007; Gaibler et al. 2012). However, in order to quantify the feedback phenomenon—namely, to specify how much mass, angular momentum, and energy is being ejected into the surrounding via the outflow channel—it is essential to model the physics in the innermost launching area of the disk–jet system with a high resolution. It is commonly accepted that ejection and accretion are tightly connected to each other (Li 1995; Ferreira & Pelletier 1995). The study of these phenomena is also motivated by the observed correlation between accretion and ejection signatures (Cabrit et al. 1990).

Our paper discusses these topics, and will provide a relation between actual magnetization within the disk and the ejection to the accretion ratio for mass and energy.

The first numerical simulations of this kind were presented by Casse & Keppens (2002, 2004), who demonstrated how an

outflow can be self-consistently launched out of the accretion disk, accelerated to high velocity, and collimated in a narrow beam. Later, Meliani et al. (2006) studied in particular the impact of a central stellar wind on the accretion disk magnetic field inclination. The work by Zanni et al. (2007) revealed the great importance of the underlying disk diffusivity, namely, the strength of diffusivity and its directional anisotropy. Studying two limits of rather high and low diffusivity, and keeping the same (about equipartition) magnetic field strength and field structure, the authors found that a steady state of the simulation could not be reached for an arbitrary combination of these parameters. Tzeferacos et al. (2009) in particular found that the efficiency of the launching mechanism is strongly dependent on the disk magnetization.

A common assumption was that in order to launch jets, the magnetic field should be rather strong, about the equipartition value. This question was investigated in detail by Murphy et al. (2010), demonstrating that jets could be driven even with a weak magnetization of $\mu \approx 0.002$.

So far, the general mechanism of jet launching from magnetized disks has been studied by a number of authors. However, due to the complexity of the problem, the combined action of the various processes engaged could not be easily disentangled. Another problem arises if only a short-term evolution of the system is considered, as this will be strongly dependent on the initial conditions. What is somewhat complicating the interpretation of simulations in the literature is that the model setup is usually categorized by the initial parameters, and not by the actual quantities such as the actual disk magnetization, accretion velocity, etc. at a certain evolutionary time. The latter was first discussed by Sheikhzadeh et al. (2012), however, the parameter space applied in those simulations was rather limited. In the present study, we will show that it is the actual disk properties, in particular, the disk magnetization, that govern the accretion and ejection.

Accretion disks are considered to be highly turbulent for any degree of the disk magnetization. The source of the turbulence is still debated, however, a great variety of unstable modes in magnetized accretion disks exists (Keppens et al. 2002). In the case of moderately magnetized disks, the main candidate is the magneto-rotational instability (MRI; Balbus & Hawley 1991; Fromang 2013). Highly magnetized disks are subject to the Parker instability (Gressel 2010; Johansen & Levin 2008) and the trans-slow Alfvén continuum modes (Goedbloed et al. 2004). The puzzling question is the following: what is the effective diffusivity and viscosity the disk turbulence provides, and how can these effects be properly implemented under the mean field approach?

As shown by Hawley et al. (1995) and later adapted by Casse & Keppens (2004); Meliani et al. (2006), the turbulent energy and angular momentum flux is dominated by the magnetic stress rather than the Reynolds stress. Thus, in the presence of a moderately strong magnetic field, the Reynolds stress becomes less important. In order to disentangle the complex behavior and keep the simulations simple, we explore only non-viscous disks.

Considering the accretion–ejection scenario, we are convinced that before any general relation between physical quantities can be claimed, it is essential that the system itself has dynamically evolved over a sufficiently extended period of time. We have therefore evolved our simulations for at least 10,000 dynamical times. We will show that such a long simulation requires that the advective and diffusive processes must be well balanced.

In our paper, we apply the following approach. First, we consider the standard diffusivity model (see, e.g., Zanni et al. 2007). After having obtained a near equilibrium solution with advection and diffusion in balance, we closely examine the state of the system. Essentially, we will argue that it is the balance between diffusion and advection that governs the strength of the actual disk magnetization. The latter appears to be the key ingredient for the evolution of the entire system. Exploring a wide range of the actual disk magnetization allows us to derive a general correlation between the actual disk magnetization and major quantities of the disk–jet system, such as the mass and energy ejection efficiencies.

We also present a model setup that is well suited for a long-term evolution study of the jet launching problem. The use of spherical geometry provides a high resolution in the inner region of the disk—the site of jet launching—and a low resolution for the outer regions, where the physical processes typically evolve on much longer timescales.

Our paper is organized as follows. Section 2 describes the numerical setup, the initial and boundary conditions of our simulations. In Section 3, we discuss our reference simulation, which is characterized by the balance between advection and diffusion, and uses the standard diffusivity model. In Section 4, we present a detailed analysis of jet launching disks, revealing the major role of the disk magnetization in the disk–jet evolution. In Section 5, we discuss simulations applying a new diffusivity model that essentially overcomes the accretion instability observed in the previous simulations. This allows us to follow the evolution of the disk–jet system substantially longer. Finally, we summarize our results in Section 6

2. MODEL APPROACH

We apply the MHD code PLUTO (Mignone et al. 2007), version 4.0, solving the time-dependent, resistive MHD equations on a spherical grid (R, Θ) . We refer to (r, z) as cylindrical

coordinates. The code numerically solves the equations for the mass conservation,

$$\frac{\partial \rho}{\partial t} + \nabla \cdot (\rho \mathbf{V}) = 0, \quad (1)$$

with the plasma density ρ and flow velocity \mathbf{V} , the momentum conservation,

$$\frac{\partial \rho \mathbf{V}}{\partial t} + \nabla \cdot \left[\rho \mathbf{V} \mathbf{V} + \left(P + \frac{\mathbf{B} \cdot \mathbf{B}}{2} \right) \mathbf{I} - \mathbf{B} \mathbf{B} \right] + \rho \nabla \Phi_g = 0 \quad (2)$$

with the thermal pressure P and the magnetic field \mathbf{B} . The central object of point mass M has a gravitational potential $\Phi_g = -GM/R$. Note that equations are written in non-dimensional form, and, as usual, the factor 4π is neglected. We apply a polytropic equation of state, $P \propto \rho^\gamma$, with the polytropic index $\gamma = 5/3$.

The code further solves for the conservation of energy,

$$\begin{aligned} \frac{\partial e}{\partial t} + \nabla \cdot \left[\left(e + P + \frac{\mathbf{B} \cdot \mathbf{B}}{2} \right) \mathbf{V} - (\mathbf{V} \cdot \mathbf{B}) \mathbf{B} + \bar{\eta} \mathbf{J} \times \mathbf{B} \right] \\ = -\Lambda_{\text{cool}}, \end{aligned} \quad (3)$$

with the total energy density,

$$e = \frac{P}{\gamma - 1} + \frac{\rho \mathbf{V} \cdot \mathbf{V}}{2} + \frac{\mathbf{B} \cdot \mathbf{B}}{2} + \rho \Phi_g, \quad (4)$$

given by the sum of thermal, kinetic, magnetic, and gravitational energy, respectively. The electric current density is denoted by $\mathbf{J} = \nabla \times \mathbf{B}$. As shown by Tzeferacos et al. (2013), cooling may indeed play a role for jet launching, influencing both jet density and velocity. For the sake of simplicity, we set the cooling term equal to Ohmic heating, $\Lambda_{\text{cool}} = -\bar{\eta} \mathbf{J} \cdot \mathbf{J}$. Thus, all generated heat is instantly radiated away.

The magnetic field evolution is governed by the induction equation

$$\frac{\partial \mathbf{B}}{\partial t} = \nabla \times (\mathbf{V} \times \mathbf{B} - \bar{\eta} \mathbf{J}). \quad (5)$$

Our simulations are performed in two-dimensional axisymmetry applying spherical coordinates. We use the Harten–Lax–van Leer Riemann solver together with a third-order Runge–Kutta scheme for time evolution and the PPM (piecewise parabolic method) reconstruction of Colella & Woodward (1984) for spatial integration. The magnetic field evolution follows the method of Constrained Transport (Londrillo & del Zanna 2004).

2.1. Numerical Grid and Normalization

No physical scales are introduced in the equations above. The results of our simulations will be presented in non-dimensional units. We normalize all variables, namely P , ρ , \mathbf{V} , and \mathbf{B} , to their values at the inner disk radius R_0 . Lengths are given in units of R_0 , corresponding to inner disk radius. Velocities are given in units of $V_{K,0}$, corresponding to the Keplerian speed at R_0 . Thus, $2\pi T$ corresponds to one revolution at the inner disk radius. Densities are given in units of ρ_0 , corresponding to R_0 . Pressure is measured in $P_0 = \epsilon^2 \rho_0 V_0^2$.

We thus may apply our scale-free simulations to a variety of jet sources. In the following, we show the physical scaling concerning three different object classes—brown dwarfs (BDs), YSOs, and AGNs. In order to properly scale the simulations, we

Table 1
Typical Parameter Scales for Different Sources

	YSOs	BDs	AGNs	Unit
R_0	0.1	0.01	20	AU
M_0	1	0.05	10^8	M_\odot
ρ_0	10^{-10}	10^{-13}	10^{-12}	g cm^{-3}
V_0	94	66	6.7×10^4	km s^{-1}
B_0	15	0.5	1000	G
T_0	1.7	0.25	0.5	days
\dot{M}_0	3×10^{-5}	2×10^{-10}	10	$M_\odot \text{ yr}^{-1}$
\dot{J}_0	3.0×10^{36}	1.5×10^{30}	3×10^{51}	dyne cm
\dot{E}_0	1.9×10^{35}	6.7×10^{29}	2.6×10^{46}	erg s^{-1}

Note. Simulation results will be given in code units and can be scaled for astrophysical application.

vary the following masses for the central object, $M = 0.05 M_\odot$ (BD), $M = 1 M_\odot$ (YSO), $M = 10^8 M_\odot$ (AGN), and thus define a scale for the inner disk radius of

$$\begin{aligned} R_0 &= 0.1 \text{ AU} \quad (\text{YSO}) \\ &= 0.01 \text{ AU} \quad (\text{BD}) \\ &= 20 \text{ AU} \left(\frac{R_0}{10 R_S} \right) \left(\frac{M}{10^8 M_\odot} \right) \quad (\text{AGN}), \end{aligned} \quad (6)$$

where $R_S = 2GM/c^2$ is the Schwarzschild radius of the central black hole. For consistency with our non-relativistic approach, we require $R_0 > 10R_S$, implying that we cannot treat highly relativistic outflows. Table 1 summarizes the typical scales for leading physical variables. For more detailed scaling laws, we refer to Appendix A.

We apply a numerical grid with equidistant spacing in the θ direction, but stretched cell sizes in the radial direction, considering $\Delta R = R\Delta\theta$. Our computational domain of a size $R = [1, 1500R_0]$, $\theta = [0, \pi/2]$ is discretized with $(N_R \times N_\theta)$ grid cells. We use a general resolution of $N_\theta = 128$. In order to cover a factor 1500 in radius, we apply $N_R = 600$. This gives a resolution of 16 cells per disk height (2ϵ) in the general case. However, we have also performed a resolution study applying a resolution two times as high (or low), thus using 256×1200 (or 64×300) cells for the whole domain, or 35 (9) cells per disk height. We satisfy the Courant–Friedrichs–Lewy condition by using a CFL number of 0.4.

2.2. Initial Conditions

For the initial conditions, we follow a meanwhile standard setup, which has been applied in a number of previous publications (Zanni et al. 2007; Sheikhezami et al. 2012; Fendt & Sheikhezami 2013). The initial structure of the accretion disk is calculated as the solution of the steady state force equilibrium,

$$\nabla P + \rho \nabla \Phi_g - \mathbf{J} \times \mathbf{B} - \frac{1}{R} \rho V_\phi^2 (\mathbf{e}_R \sin \theta + \mathbf{e}_\theta \cos \theta) = 0. \quad (7)$$

We solve this equation assuming radial self-similarity, i.e., assuming that all physical quantities X scale as a product of a power law in R with some function $F(\theta)$,

$$X \equiv X_0 R^{\beta_X} F(\theta). \quad (8)$$

Self-similarity requires in particular that the sound speed and the Alfvén speed scales as the Keplerian velocity, $V_K \propto r^{-1/2}$, along the disk midplane. As a consequence, the power-law coefficients

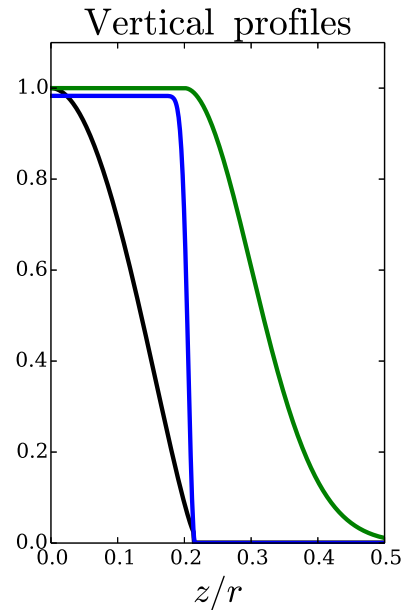


Figure 1. Initial vertical profiles of the disk quantities: density (black, blue shaded), rotational velocity (blue), and magnetic diffusivity F_η (green). The magnetic diffusivity profile is set constant in time.

(A color version of this figure is available in the online journal.)

β_X are determined as follows: $\beta_{V_\phi} = -1/2$, $\beta_P = -5/2$, $\beta_\rho = -3/2$, and $\beta_{B_R} = \beta_{B_\theta} = \beta_{B_\phi} = -5/4$.

An essential non-dimensional parameter governing the initial disk structure is the ratio ϵ between the isothermal sound speed $C_s^T = \sqrt{P/\rho}$ and the Keplerian velocity $V_K = \sqrt{GM/r}$, evaluated at the disk midplane, $\epsilon = [C_s^T/V_K]_{\theta=\pi/2}$. This quantity determines the disk thermal scale height $H_T = \epsilon r$. In our simulations, we generally initially assume a thin disk with $\epsilon = 0.1$. Note that for the remainder of the paper, when discussing the dynamical properties of disk and outflow, we consider the adiabatic sound speed $C_s = \sqrt{\gamma P/\rho}$. The geometrical disk height, namely, the region where the density and rotation significantly decrease, is about 2ϵ (see Figure 1). We therefore define the geometrical disk height as $H \equiv 2\epsilon r$.

Following Zanni et al. (2007), our reference simulation is initialized only with a poloidal magnetic field, defined via the vector potential $\mathbf{B} = \nabla \times A \mathbf{e}_\phi$, with

$$A = \frac{4}{3} B_{p,0} r^{-1/4} \frac{m^{5/4}}{(m^2 + ctg^2\theta)^{5/8}}. \quad (9)$$

The parameter $B_{p,0} = \epsilon \sqrt{2\mu_0}$ determines the strength of the initial magnetic field, while the parameter m determines the degree of bending of the magnetic field lines. For $m \rightarrow \infty$, the magnetic field is purely vertical. As we will see below, the long-term evolution of the disk–jet structure is insensitive to this parameter, since, due to advection and diffusion processes and the jet outflow, the magnetic field structure changes substantially over time. We therefore set $m = 0.5$ in general.

The strength of the magnetic field is governed by the magnetization parameter

$$\mu = \frac{B_p^2}{2P} \Big|_{\theta=\pi/2}, \quad (10)$$

the ratio between the poloidal magnetic field pressure and the thermal pressure, evaluated at the midplane, and is set to be constant with radius. As we will see below, the magnetic

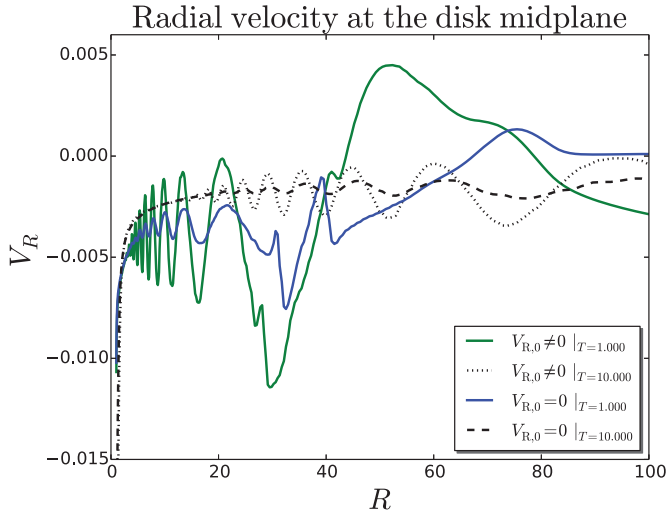


Figure 2. Accretion velocity profile along the disk midplane at $T = 1000$ and $T = 10,000$ for the cases of zero and non-zero initial radial velocity.

(A color version of this figure is available in the online journal.)

field distribution substantially changes over time, while the disk-jet dynamics is governed by the actual disk magnetization. Typically, the initial magnetization is $\mu_0 \approx 0.01$ in this simulations.

Outside the disk, the gas and pressure distribution is defined as hydrostatic “corona,”

$$\rho_{\text{cor}} = \rho_{\text{cor},0} R^{-1/(\gamma-1)}, \quad P_{\text{cor}} = \frac{\gamma-1}{\gamma} \rho_{\text{cor},0} R^{-\gamma/(\gamma-1)}, \quad (11)$$

where $\rho_{\text{cor},0} = \delta \rho_{\text{disk}}(R=1, \theta = \pi/2)$ with $\delta = 10^{-3}$.

Although it is common to define the initial accretion velocity, balancing the imposed diffusivity $V_R = \eta J_\phi / B_\theta$, we find that this is not necessary in our set of parameters. It can even disturb the initial evolution of the disk accretion. Accretion requires corresponding torques to be sustained and since there is no initial poloidal current defined, $B_\phi = 0$ (which takes time to build up from a weak poloidal field), a non-zero initial velocity will only lead to extra oscillations. Figure 2 illustrates this issue, showing two identical simulations with zero and non-zero accretion velocity. We found that the origin of the oscillations for both cases is the inner boundary. The first wave of accretion is somehow bounced outward by the inner boundary and results in an oscillatory pattern. We believe that the bouncing at the inner disk boundary can be caused by small inconsistencies between the boundary conditions and the intrinsic disk physics, a problem that may be present in other studies. Although they both result in the same final profile (a steady state has been reached only for small disk radii), the simulations with zero velocity profiles show fewer oscillations.

2.3. Boundary Conditions

We apply standard symmetry conditions along the rotational axis and the equatorial plane. Along the radial boundaries of the domain, we distinguish two different areas. That is (1) a disk boundary for $\theta > (\pi/2) - 2\epsilon$ ¹ and (2) a coronal boundary for $\theta < (\pi/2) - 2\epsilon$, and consider different conditions along them (see Figure 3).

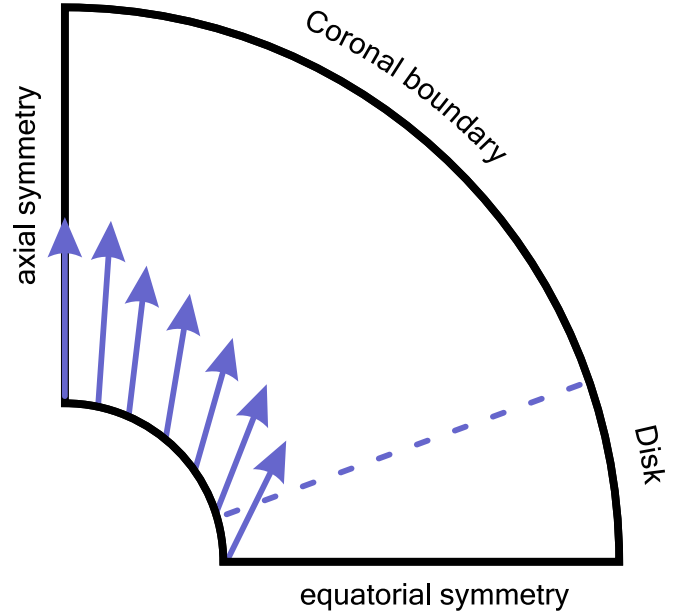


Figure 3. Illustration of the boundary conditions. Along the inner and outer radial boundaries, we distinguish two zones—the corona and the disk region. Arrows represent the magnetic field distribution along the inner boundary, which is preserved by our boundary condition.

(A color version of this figure is available in the online journal.)

Along the inner radial boundary for all simulations, we impose a constant slope for the poloidal component of the magnetic field

$$\varphi = 70^\circ \left(1 + \exp \left(- \frac{\theta - 45^\circ}{15^\circ} \right) \right)^{-1}, \quad (12)$$

where φ is the angle with respect to the unit vector \mathbf{e}_R . The magnetic field direction is axial near the axis, $\theta = 0$, while at the inner disk radius the inclination is 70° with respect to the disk surface. A smooth variation of the magnetic field direction is prescribed along the inner radial boundary. This is in concordance with Pelletier & Pudritz (1992), who showed that for a warm plasma the maximum angle with respect to the disk surface necessary to launch outflows is about 70° , and slightly larger than for a cold plasma (Blandford & Payne 1982).

The method of constraint transport requires the definition of only a tangential component, thus to prescribe B_θ along the innermost boundary, while the normal component B_R follows from solving $\nabla \cdot \mathbf{B} = 0$. In order to implement the prescription of a constant magnetic field angle, we solve $\nabla \cdot \mathbf{B} = 0$, taking into account the ratio of the cell-centered magnetic field components $B_\theta / B_R = -\tan(\varphi)$. We start the integration from the axis ($\theta = 0$), where $B_\theta = 0$. Thus, by fixing the slope of the magnetic lines, we allow the magnetic field strength to vary.

Along the inner coronal boundary, we prescribe a weak inflow into the domain with $V_p = 0.2$. This is applied to stabilize the inner coronal region between the rotational axis and the disk jet, since the interaction between the current carrying, magnetized jet and zero- B_ϕ coronal region may lead to some extra acceleration of the coronal gas. As shown by Meliani et al. (2006), the pressure of such an inflow (e.g., a stellar wind) may influence the collimation of the jet, changing the shape of the innermost magnetic field lines.

In order to keep the influence of the dynamical pressure of the inflow similar during the whole evaluation (and also for

¹ Note, $2\epsilon \approx \arctg(2\epsilon)$.

Table 2
Inner and Outer Boundary Conditions

	ρ	P	V_R	V_θ	V_ϕ	B_R	B_θ	B_ϕ
Inner disk	$\sim r^{-3/2}$	$\sim r^{-5/2}$	$\sim r^{-1/2}, \leq 0$	0	$\sim r^{-1/2}$	Slope	Slope	$\sim r^{-1}$
Inner corona	$\sim r^{-3/2}$	$\sim r^{-5/2}$	$0.2 \cos(\varphi)$	$0.2 \sin(\varphi)$	$\sim r^{-1/2}$	Slope	Slope	0
Outer disk	$\sim r^{-3/2}$	$\sim r^{-5/2}$	Outflow, ≤ 0	Outflow	Outflow	div B = 0	Outflow	$\sim r^{-1}$
Outer corona	$\sim r^{-3/2}$	$\sim r^{-5/2}$	Outflow, ≥ 0	Outflow	Outflow	div B = 0	Outflow	$\sim r^{-1}$

Note. Outflow is the zero gradient condition and the constant slope conditions are marked by “slope” in the table.

different simulations), we set the density of this inflow with respect to the disk density at the inner disk radius. The density of the inflow corresponds to a hydrostatic corona $\rho_{\text{infl}} = \rho_{\text{cor}} = \rho_{\text{disk}}|_{\text{midplane}}(t) \cdot \delta$, where $\delta = 10^{-3}$. The inflow direction is aligned with the magnetic field direction. By choosing a denser inflow, we also increase the time step of our simulations by approximately three times, as the Alfvén speed in the coronal region lowers.

By varying the slope of the magnetic field φ along this inner corona in the range of 60–80 deg, we found that it only slightly affects the slope of the innermost magnetic field lines. The global structure of the magnetic field is instead mainly governed by the diffusivity model. Since the inner boundary by design models the magnetic barrier of the star, we choose a rather steep slope in order to avoid the disk magnetic flux entering the coronal region.

Across the inner disk boundary (that is the accretion boundary), density and pressure are both extrapolated by power laws, applying $\rho R^{-3/2} = \text{const}$ and $PR^{-5/2} = \text{const}$, respectively. Both the toroidal magnetic field as well as the toroidal velocity components are set to vanish at the inner coronal boundary, $B_\phi = 0$, $V_\phi = 0$. For the inner disk boundary, we further apply the condition $B_\phi \sim 1/r$ ($J_\theta = 0$), and extrapolate the radial and the toroidal velocity by power laws, $V_R R^{-1/2} = \text{const}$, and $V_\phi R^{-1/2} = \text{const}$, respectively, while $V_\theta = 0$.

For the inner disk boundary, only negative radial velocities are allowed, making the boundary to behave as a “sink,” thus absorbing all material that is delivered by the accretion disk at the inner disk radius.

As the application of spherical coordinates provides an opportunity to use a much larger simulation domain compared to cylindrical coordinates, the outer boundary conditions have little influence on the evolution of the jet launched from the very inner disk. We therefore extrapolate ρ and P with the initial power laws and apply the standard PLUTO outflow conditions for V_R , V_θ , and V_ϕ at the outer boundary, thus, zero gradient conditions. We further require $B_\phi \sim 1/r$ ($J_\theta = 0$) for the toroidal magnetic field component, while a simple outflow condition is set for B_θ . Again, B_R is obtained from the $\nabla \cdot \mathbf{B} = 0$.

For the radial velocity component, we distinguish between the coronal region, where we require positive velocities $V_R \geq 0$, and the disk region, where we enforce negative velocities $V_R \leq 0$.

As our application of a spherical geometry is new in this context, we summarize the boundary conditions in the Table 2.

2.4. The Magnetic Diffusivity Model

Accretion disks are considered to be highly turbulent, subject to the MRI in moderately magnetized disks (Balbus & Hawley 1991; Fromang 2013), and the Parker instability (Gressel 2010; Johansen & Levin 2008) for stronger magnetized disks. It is believed that when the magnetic field becomes sufficiently strong, the MRI modes become suppressed (Fromang 2013). On

the other hand, a strong magnetic field may become buoyant, leading to the Parker instability. While the MRI is confined within the disk, the Parker instability operates closer to the surface of the disk where the toroidal magnetic field is stronger.

Extrapolating the results from a self-consistent, local treatment of turbulence to the mean field approach is not straightforward. In the local treatment, the extraction of angular momentum is due to both turbulence—operating on small scales—and torques by the mean magnetic field on large scales. Thus, the removal of angular momentum goes hand in hand with destroying the turbulent magnetic field or the effective magnetic diffusivity. In case of the mean field approach, there is no small-scale turbulence and, thus, no angular momentum removal by local turbulent motions. Here, the diffusivity plays only a role for leveling the magnetic field gradient, thus setting the overall structure of the magnetic field. Unfortunately, we lack complete knowledge of the disk turbulence, thus the connection between the mean magnetic field and the fluctuating part, or, in other words, the relation between the mean magnetic field and the effective torques, and the diffusivity and viscosity that turbulence provides. We believe that when moving from a local turbulence approach to the mean field approach, the relevance of the model should be approved by the relevance of the magnetic field distribution itself, and not by the diffusivity model. However, one should keep in mind that the magnetic field strength and structure of real accretion disks are also not known. Therefore, when considering any simulation results, the diffusivity model applied should always be taken into account.

A self-consistent study of the origin of the turbulence is beyond the scope of our paper. We therefore prescribe a certain model of the magnetic diffusivity. We apply an α -prescription (Shakura & Sunyaev 1973) for the magnetic diffusivity, implicitly assuming that the diffusivity has a turbulent origin. The diffusivity profile may extend up to one disk height above the disk surface (Figure 1).

Although we investigate different diffusivity models, all of them can be represented in a following form

$$\eta_P = \alpha_{\text{ssm}}(\mu) C_s \cdot H \cdot F_\eta(z), \quad (13)$$

where the vertical profile of the diffusivity is described by a function

$$F_\eta(z) = \begin{cases} 1 & z \leq H \\ \exp\left(-2\left(\frac{z-H}{H}\right)^2\right) & z > H, \end{cases}$$

confining the diffusivity to the disk region.

Although this parameterization of diffusivity is commonly used (except the profile function $F_\eta(z)$), there are no clear constraints upon the value α_{ssm} may take. As an example, King et al. (2007) discuss a magnitude of the turbulent α -parameter derived from observations and simulations, indicating observational values $\alpha_{\text{ssm}} \simeq 0.1..0.4$. Numerical models

with zero net magnetic field usually provide low numerical values $\alpha_{\text{ssm}} \simeq 0.01$, reaching at most $\alpha_{\text{ssm}} \simeq 0.03$ (Stone et al. 1996; Beckwith et al. 2011; Simon et al. 2012; Parkin & Bicknell 2013). On the other hand, numerical modeling of the MRI applying a non-zero net magnetic field (Bai & Stone 2013) indicates substantially higher values, $\alpha_{\text{ssm}} \simeq 0.08$ –1.0, with a corresponding magnetization $\mu = 10^{-4}$, 10^{-2} .

Obviously, different functions of $\alpha_{\text{ssm}}(\mu)$ will lead to different evolution. We start from the well-known model for magnetic diffusivity applied by many authors previously (Casse & Keppens 2004; Zanni et al. 2007; Sheikhezami et al. 2012),

$$\eta_{\text{P}} = \alpha_{\text{m}} V_{\text{A}} \cdot H \cdot F_{\eta}(z) \quad (14)$$

by applying $\alpha_{\text{ssm}} = \alpha_{\text{m}} \sqrt{2\mu}$, where $V_{\text{A}} = B_{\text{P}}/\sqrt{\rho}$ is the Alfvén speed, and μ , C_{s} , and H are the magnetization, the adiabatic sound speed, and the local disk height, respectively, measured at the disk midplane. We evolve α_{ssm} and C_{s} in time, but for the sake of simplicity, we keep H and $F_{\eta}(z)$ constant in time, thus equal to the initial distribution. The main reason is to avoid additional feedback, which favors the accretion instability (see below, or, e.g., Campbell 2009). Our test simulations evolving the disk height in time in fact indicate the rise of such instability earlier than in the case of a fixed-in-time disk diffusivity aspect ratio.

2.5. Anisotropic Diffusivity

In general, the diffusivity tensor has diagonal non-zero components,

$$\eta_{\phi\phi} \equiv \eta_{\text{P}} \quad \eta_{\text{RR}} = \eta_{\theta\theta} \equiv \eta_{\text{T}}, \quad (15)$$

where we denote η_{P} as the poloidal magnetic diffusivity, and η_{T} as the toroidal magnetic diffusivity, respectively.² The anisotropy parameter $\chi \equiv \eta_{\text{T}}/\eta_{\text{P}}$ quantifies the different strength of diffusivity in poloidal and toroidal directions.

In the literature, it is common to assume χ of the order of unity. Considering viscous disks, Casse & Ferreira (2000) showed that there is a theoretical limit for η_{T} , namely $\eta_{\text{T}} > \eta_{\text{P}}$. Highly resolved disk simulations indeed suggest $\chi \simeq 2 \dots 4$ (Lesur & Longaretti 2009), implying that the toroidal field component is typically diffusing faster than the poloidal component.

The majority of simulations in the literature consider a magnetic field strength in equipartition with the gas pressure. However, also studying weakly magnetized disks, we find that there also exists an upper limit for the anisotropy parameter, above which the simulations show irregular behavior. On the other hand, it was pointed out by several authors (see, e.g., Zanni et al. 2007) that in case of a very low anisotropy parameter (thus, a weak toroidal diffusivity), the simulations might suffer from instabilities caused by strong pinching forces. Nonetheless, the existence of an upper limit for the anisotropy parameter was so far obscured by other processes.

Assuming a steady state and combining the poloidal component of the diffusion equation, $M_{\text{R}} = \alpha_{\text{ssm}} H J_{\phi}/B_{\text{P}}$, with the relation for the Mach number $M_{\text{R}} = 2/\sqrt{\gamma} H J_{\text{R}}/B_{\text{P}} \mu_{\text{act}}$ (see

below, Königl & Salmeron 2011), an interrelation between the toroidal and poloidal electric currents can be derived,

$$\frac{J_{\phi}}{J_{\text{R}}} = \frac{\sqrt{2\mu}}{\sqrt{\gamma}\alpha_{\text{m}}}. \quad (16)$$

This relation has been proven to approximately hold for all of our simulations, thus indicating that a steady state has indeed been reached. Since the only free parameter in this relation is α_{m} , the choice of α_{m} governs the ratio of the electric current components.

As shown previously (Ferreira & Pelletier 1995; Ferreira 1997; Ferreira & Casse 2013), the toroidal component of the induction equation can be written as

$$\eta_{\text{T}} J_{\text{R}}|_{\text{mid}} = -R^2 \int_0^{2\epsilon} \mathbf{B}_{\text{P}} \cdot \nabla \Omega d\varphi - V_{\theta} B_{\phi} \quad (17)$$

(here expressed for spherical coordinates), where J_{R} is computed at the disk midplane. This equation essentially states that the induction of the toroidal magnetic field component (from twisting the poloidal component) is balanced by the diffusion through the disk midplane and by the flux escaping through the disk surface. We emphasize that we do not neglect the $V_{\theta} B_{\phi}$ term, considering the assumption of a thin disk (Ferreira & Casse 2013), as we find it of key importance in our simulations, in particular in the regime of a moderately strong magnetic field, $\mu \geq 0.1$.

Assuming that the induction of the magnetic field is primarily due to radial gradients, the radial component of the magnetic field can be approximated by a power law, $B_{\text{R}} \propto R^{-5/4}$, and Equation (17) may be transformed into $\eta_{\text{T}} J_{\text{R}}|_{\text{mid}} \simeq B_{\text{R}} C_{\text{s}} - V_{\theta} B_{\phi}$, or

$$(\alpha_{\text{ssm}} \chi - M_{\theta}) J_{\text{R}} \simeq \frac{B_{\text{R}}}{H}, \quad (18)$$

where

$$M_{\theta} = -V_{\theta}^+ / C_{\text{s}} \quad (19)$$

is denoted as the ejection Mach number, where V_{θ}^+ is measured at the disk surface.

Using relation 16 between the poloidal and toroidal electric currents and defining the curvature part of the toroidal current $J_{\phi}^{\text{curv}} \equiv B_{\text{R}}/H$, one may derive a constraint for the anisotropy parameter,

$$\frac{J_{\phi}^{\text{curv}}}{J_{\phi}} \simeq \left(\alpha_{\text{m}} \chi - \frac{M_{\theta}}{\sqrt{2\mu}} \right) \alpha_{\text{m}} \leq 1. \quad (20)$$

Any magnetic field geometry that is outwardly bent and has a decreasing field strength in the outward direction has to satisfy this relation, as J_{ϕ} consists of two positive terms, the gradient and the curvature. In cases where the vertical velocity term can be neglected (e.g., for a very weak magnetic field with $\mu \leq 0.02$), the anisotropy parameter is $\chi < 1/\alpha_{\text{m}}^2$, which, for our choice of α_{m} , is about 0.4. By probing the χ parameter space, we found that in order to obtain a stable accretion-outflow configuration for weakly magnetized disks, the χ should be in the range 0.3–0.7. We therefore decided to apply $\chi = 0.5$ for all of our simulations. We note that in simulations applying an anisotropy parameter $\chi \geq 0.7$, we faced the problem that the poloidal magnetic field lines were “moving” rapidly, such that the bending of the field lines along the disk midplane was actually inverted. This is a result of the combined effects of

² Note that our notation of toroidal and poloidal diffusivity follows the actual use in axisymmetric jet formation simulations. A more general notation, applicable also in three dimensions, would be that of azimuthal and meridional diffusivity.

Table 3
Comparison of Our Simulations with Simulations Performed by Other Authors

Reference	Cell/ 2ϵ	ϵ	m	α_m	χ	μ_0	μ_{act}
Casse & Keppens (2004)	0.5	0.1		<1	1	$\simeq 1$...
Zanni et al. (2007)	2.5	0.1	0.35	0.1 ... 1.0	1, 3	0.3	...
Tzeferacos et al. (2009)	2.5	0.1	0.4	0.1 ... 1.0	3, 100	0.1–3.0	...
Sheikhnezami et al. (2012)	8.0	0.1	0.4	1.0	1/3, 3	0.002–0.1	...
This work, reference simulation	16	0.1	0.2–0.9	1.1–1.9	0.5	0.003–0.03	0.001–0.5
This work, resolution study	24.5	0.1	0.2–0.9	1.1–1.9	0.5	0.003–0.03	0.001–0.5

Note. The resolution is estimated for the inner disk ($R = 1$).

a strong outward diffusion and low torques at the midplane. On the other hand, in case of a rather low anisotropy parameter, the accretion is rapid and the jet does establish a steady behavior.

The reason why the commonly chosen anisotropy $\chi > 1$ leads to a steady behavior is rather simple. As the disk magnetization grows during advection, the ejection Mach number grows as well (we find that $M_\theta \propto 6\mu$ saturating at a level of 0.8; see below). Thus, in the case of a high disk magnetization—usually assumed in the literature—the above-mentioned upper limit for the anisotropy parameter is satisfied. In the case of weak magnetic field simulations, performed, for example, by Murphy et al. (2010), this limit is most likely satisfied by additional viscous torques.

2.6. Comparison to Previous Simulations

In the Introduction we have already discussed the literature of accretion–ejection simulations. Here we want to explicitly emphasize specific details in which our simulations differ from previous works.

1. A spherical grid has been applied, offering the opportunity of a much larger domain size as well as much higher resolution in the inner part of the disk. A new set of boundary conditions is used which is adapted to the spherical grid.
2. We were able to explore a continuous range of simulation parameters. In particular, we were aiming to disentangle interrelations between the actual flow parameters, rather than an interrelation to the initial values.
3. Altogether, our model setup allows very long-term simulations on a large grid—so far we have run simulations for approximately 30,000 time units for a standard diffusivity model, and more than 150,000 time units for our modified strong diffusivity model.
4. We allow the inflow (into the coronal region) density to vary in time, thus keeping the ratio between the inflow and the disk densities δ the same as initially.

We have explored a vast range of the parameter space that covers the majority of simulations performed in the literature (see Table 3). Similar to all these papers, we assume a thin disk $\epsilon = 0.1$. It is common to assume a magnetic diffusivity parameter α_m of about unity. In our case, we apply values $\alpha_m = 1.1 \dots 1.9$. For the magnetic field bending parameter, we have chosen $m = 0.5$, which is slightly higher than the values usually adapted, $m = 0.35 \dots 0.4$. Although we finally show that m plays only a minor role, our choice is motivated by the fact that this value is more consistent with the inner boundary condition. The magnetic diffusivity anisotropy parameter χ is chosen to be smaller than unity, since it helps to keep sufficiently strong torques at the midplane and the bending of the magnetic field that supports launching.

Although we begin our simulation from a moderately weak initial magnetic field, the actual field strength in the inner disk at a certain radius may vary substantially over time. This allows us to study the interrelation between disk accretion and ejection physics and the actual magnetic field strength (thus the actual disk magnetization).

3. A REFERENCE SIMULATION

In this section, we present our reference simulation. Our aims were two-fold. First, with our new setup we were able to increase both the period of time evolution and the spatial extension of jet-launching conditions considerably compared to previous works. Second, with our long-term evolution simulations, we were able to investigate the interrelation between the actual disk properties such as magnetization, the ejection to accretion ratios of mass and energy, jet velocity, and others. This has not been done in the past, as most papers have compared the initial parameters of the simulations. As shown by Sheikhnezami et al. (2012), both the magnetization and diffusivity may substantially change during the disk evolution, and the parameters for the initial setup μ_0 or α_{ssm} are not sufficient to characterize the disk–jet system.

In order to uniquely specify the initial conditions for the simulation, we prescribe a number of non-dimensional characteristic parameters. The initial disk height is set by ϵ . For all simulations, we apply $\epsilon = 0.1$. The initial strength and structure of the magnetic field is set by μ_0 and m , respectively. In all simulations, we have chosen $m = 0.5$.

As we will show below, the initial disk magnetization can fail to characterize the jet-launching process, but it is responsible for the overall disk torques. The main reason is that the magnetization in the inner disk, from which the main jet is being launched, changes very quickly. However, the magnetic field in the overall disk is primarily set by the initial magnetization.

In our simulations, we examine $\mu_0 = (0.003, 0.01, 0.03)$.

The model for diffusivity is chosen by selecting the distribution $\alpha_{\text{ssm}}(\mu)$ and the anisotropy parameter χ . We also set $\chi = 0.5$ for all simulations. We apply a standard diffusivity model (Equation (14)), thus the diffusivity is set by the α_m parameter. As will be shown later, the simulations are very sensitive to this parameter. If not stated otherwise, $\alpha_m = 1.65$.

We will refer to our reference simulation as to the setup with $\epsilon = 0.1$, $m = 0.5$, $\mu_0 = 0.01$, $\alpha_m = 1.65$, $\chi = 0.5$. Usually we run the simulations until $t = 10,000$, corresponding to about 1600 orbits at the inner disk radius.

Figure 4 shows the time evolution of the disk–jet structure of the reference simulation. Note that here we present only a small cylindrical part of a much larger, spherical domain. Although we explore a broad parameter space, the evolution for this simulation can be seen as typical.

The first snapshot shows the initial state—a hydrodynamic disk in force-balance, the non-rotating hydrostatic corona in

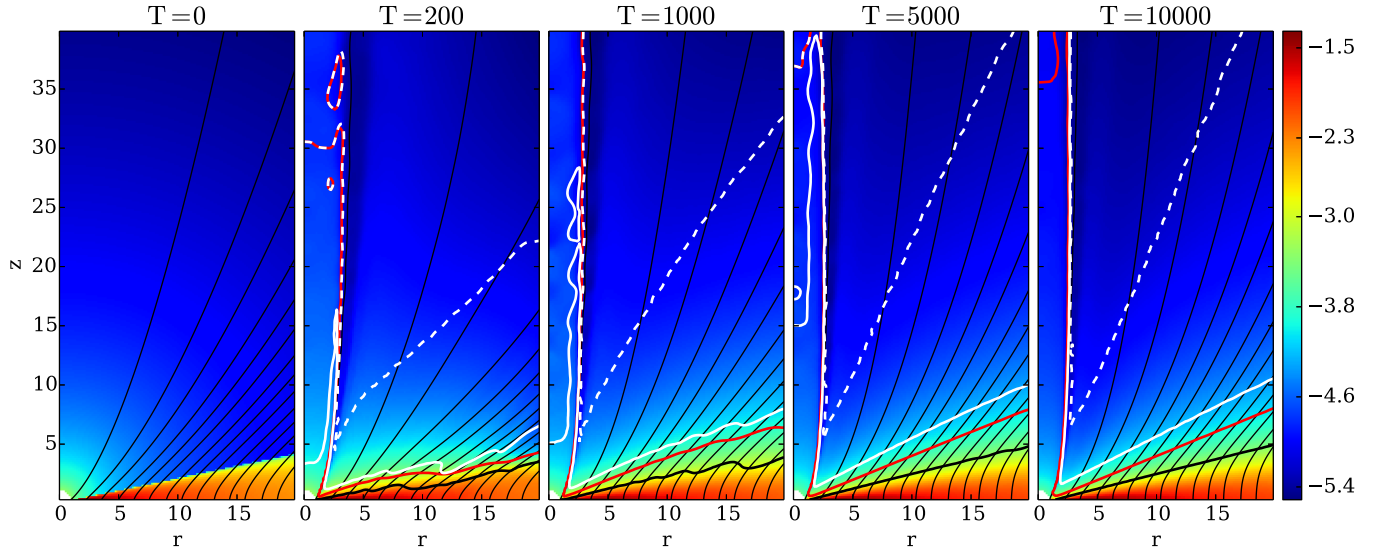


Figure 4. Time evolution of the disk-jet structure for the reference simulation. Shown is the evolution of the density (by colors, in logarithmic scale), the poloidal magnetic field lines (thin black lines), the disk surface (thick black line), the sonic (red line), the Alfvén (white line), and the fast Alfvén (white dashed line) surfaces. (A color version of this figure is available in the online journal.)

pressure equilibrium with the disk, and the initial non-force-free magnetic field. After some 1000 revolutions, the inner parts of the disk-outflow reaches a quasi-steady state. However, it takes a much longer time for the outer parts to reach such a state. The outflow, initiated at early times and constantly accelerated, finally reaches a super-fast magnetosonic speed. The outflow-launching area along the disk surface grows with time. However, the parts of the outflow being launched from larger disk radii are less powerful.

This reference simulation applying typical parameters from the literature can be re-established very well by our approach. Using a spherical setup, the resolution in the inner part of the disk is higher than in the literature, and the simulations run substantially longer than any other simulation published previously. Our simulations behave very robustly. We believe that there are two main reasons for that. First, the spherical geometry does well resolve the inner part of the disk, from which the dominant part of the jet is launched, but smooths out the small-scale perturbations in the outer disk. By that, perturbations arising throughout the disk are diminished. Second, our choice for the diffusivity parameter α_m allows the simulations to evolve into a quasi-steady state in which advection is balanced by diffusion. However, even with such an optimized numerical setup (the reference setup), our simulations show some irregular behavior typically at about 30,000 time units. The reason is that since the current diffusivity model is prone to the accretion instability (see Lubow et al. 1994, and Equation (14)), the simulations are always in a state of marginal stability. As a consequence, the simulations evolve into a state of either high or low magnetization. In case of high magnetization, the structure of the inner disk is being drastically changed and the current model of diffusivity cannot be applied. In the opposite case of weak magnetization, stable jets cannot be sustained.

In the following, we discuss different components of the disk-jet system and the jet-launching and acceleration mechanism. We define how we measure certain disk properties, such as the location of the disk surface or the mass fluxes in the physically different areas. We explore the role of the diffusivity, the strength, and geometry of the magnetic field in respect to the outflow and accretion rates.

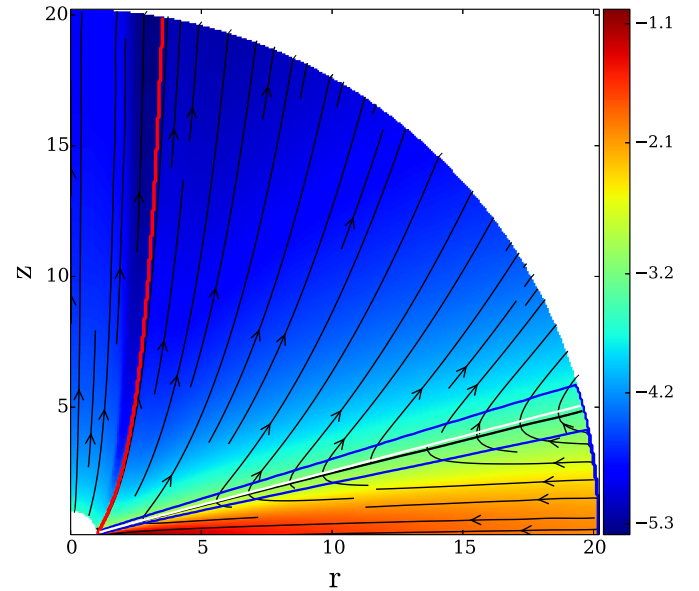


Figure 5. Physically different regions of the disk-jet structure at $t = 10,000$. Shown is the mass density (in logarithmic scale) and streamlines of the poloidal velocity (black lines with arrows). The red line marks the magnetic field line rooted at an innermost area of the midplane. The upper blue line separates an area where $V_p \parallel B_p$ from the disk. The accretion and ejection areas are separated with white ($V_r = 0$) and black ($F_\phi = 0$) lines, respectively. The lower blue line separates the accretion area where $V_r \gg V_\theta$ from the rest of the structure. (A color version of this figure is available in the online journal.)

3.1. Disk Structure and Disk Surface

We define the disk surface as a surface where the radial velocity changes sign. In a steady state, the area where the radial velocity and the magnetic torque changes sign is almost identical.

Figure 5 shows the typical structure of the disk-jet system. Several, physically different regions can be distinguished—the inflow area, the jet acceleration area, the launching area, and the accretion domain. These are separated by colored lines. The white and black lines mark the disk surface that separates disk and corona regions. Two other lines separate the accretion,

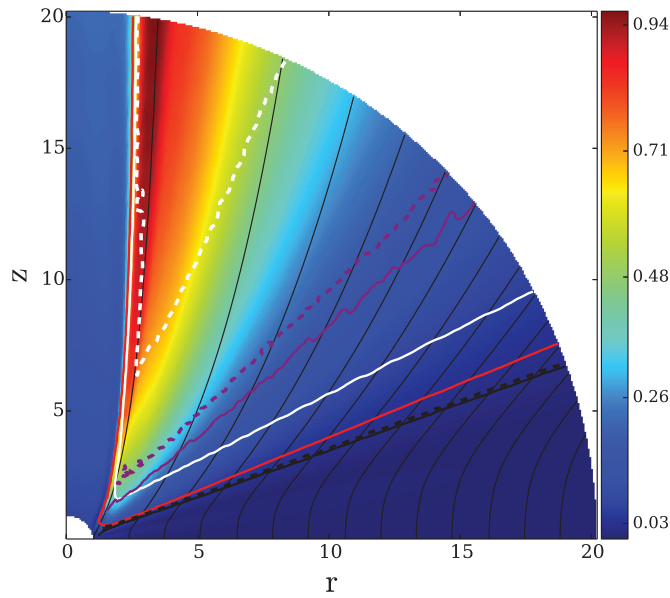


Figure 6. Importance of the Lorentz force with respect to the pressure and centrifugal forces for the reference simulation at $T = 10,000$. Shown are the poloidal speed (different colors), the poloidal magnetic field (black thin lines), Alfvén (white), fast-magnetosonic (dashed white), and sonic (red) surfaces. The thick black lines denote the surface where the Lorentz force is equal to the pressure force components: parallel (dashed) and perpendicular (solid) to the magnetic field. The thick purple lines denote the surface where the Lorentz force is equal to the centrifugal force components: parallel (dashed) and perpendicular (solid) to the magnetic field. The thick black lines denote the ratios of the Lorentz to the pressure forces components: parallel (left) and perpendicular (right) to magnetic field.

(A color version of this figure is available in the online journal.)

launching, and acceleration areas. We define the accretion region as the area where velocity is mainly radial, $V_\theta < 0.1 V_R$, and the acceleration region as the area where the flow velocity is parallel to the magnetic field, $\sin(\text{angle}(B, V)) < 0.1$. We characterize the region in between as the launching area.

In our simulations, the position of the disk surface as defined above remains about constant in time. This confirms our choice of the control volume (see below) and our choice to fix the diffusive scale height during the simulation.

According to our boundary conditions, we prescribe a weak inflow into the region between the inner disk radius and the rotational axis. This inflow provides the matter content as well as the pressure balance along the rotational axis. The astrophysical motivation can be the presence of a central stellar magnetic field or a stellar wind. In Figure 5, the inflow area is the area between the rotational axis and the red line that marks the magnetic field line rooted in the inner disk radius at the midplane. In all figures below, the magnetic field line closest to the axis always corresponds to the magnetic field line anchored at the inner disk radius.³

3.2. Launching Mechanism

Here we briefly comment on the jet-launching mechanism in our reference simulation that is—as in previous simulations—the Blandford–Payne magneto-centrifugal driving.

³ Note that there are magnetic field lines that still penetrate the disk, but are not rooted at the disk midplane. These lines originate from inside the inner disk radius and are considered as intermediate between the axial coronal region and the main disk outflow. The pure inflow, which is prescribed from the coronal region along the inner boundary, is moving with the injection speed, and thus is not accelerated.

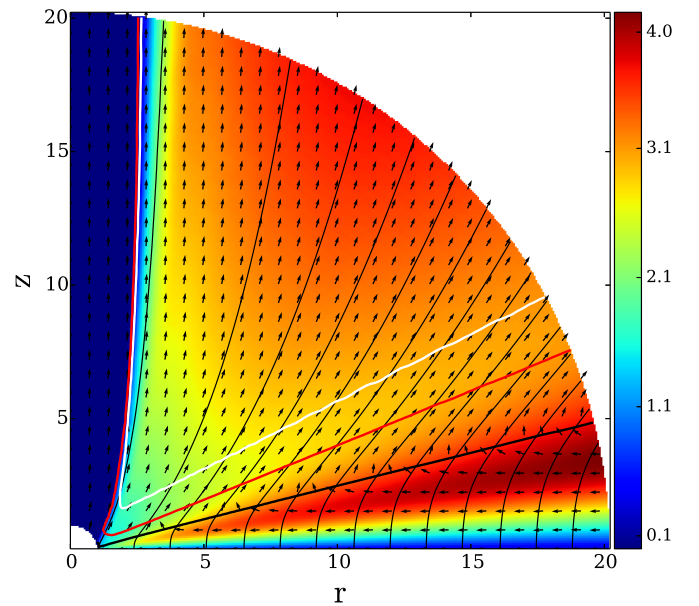


Figure 7. Ratio of the toroidal to the poloidal magnetic field for the reference simulation at $T = 10,000$. The lines represent the disk (thick black line), the sonic (red line), and the Alfvén (white line) surfaces. Arrows show the normalized velocity vectors.

(A color version of this figure is available in the online journal.)

As demonstrated above (see Figure 5), the magnetic torque $r F_\phi$ changes sign on the disk surface. It is negative in the disk and positive in the corona. Thus, the magnetic field configuration established extracts angular momentum from the disk. The angular momentum extraction relies on the induced toroidal magnetic field component, which plays a key role in transferring the angular momentum $\sim B_r B_\phi$. Gaining angular momentum, the material that is loaded to the field lines from the accretion disk is pushed outward by the centrifugal force.

In order to illustrate the acceleration process, we show the magnitude of Lorentz force with respect to the thermal pressure and centrifugal forces. Figure 6 shows the contours where the perpendicular and parallel components of the Lorentz force are equal to the perpendicular and parallel components of the pressure and centrifugal forces, respectively. In the accretion disk, both the pressure and the centrifugal forces dominate the poloidal component of the Lorentz force. Below the disk surface, the Lorentz force (toroidal component) extracts the angular momentum from the disk.

Since the Lorentz force increases along the outflow, it is worth checking the decomposed Lorentz force components $F = \nabla \times B \times B$ in the directions parallel and perpendicular to the magnetic field (Ferreira 1997). The ratio between the toroidal and parallel components of the magnetic field,

$$\frac{F_{||}}{F_\phi} = -\frac{B_\phi}{B_p}, \quad (21)$$

is shown in Figure 7. We see that the centrifugal force is stronger in the inner area of the disk rather than in the outer parts of the disk.

At the sonic surface, the Lorentz force overcomes the pressure forces. From this point on, the main acceleration force is the centrifugal force. Further along the outflow—between the Alfvén surface and the fast surface—the Lorentz force becomes the main accelerating force.

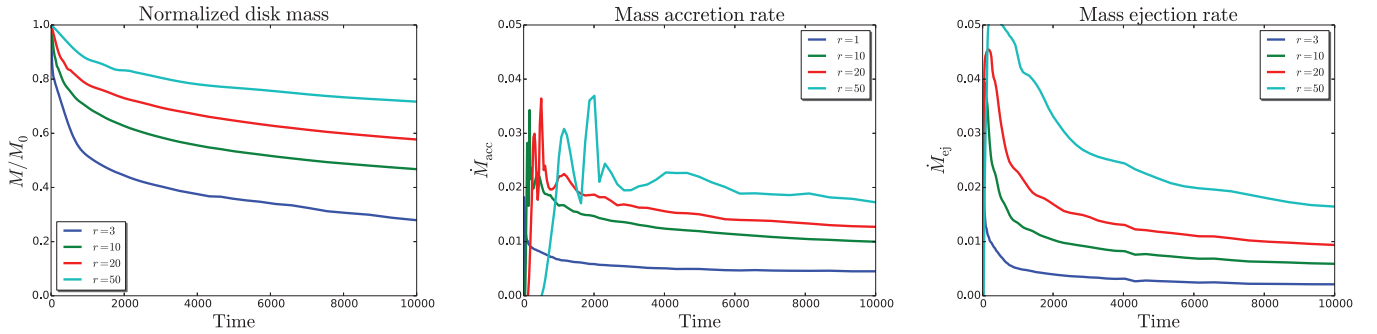


Figure 8. Time evolution of the disk mass (left), the mass accretion rate (middle), and the mass ejection rate (right) of the reference simulation at different radii. (A color version of this figure is available in the online journal.)

3.3. Mass Flux Evolution

We now explore the mass flux evolution, namely the accretion and ejection rates.

In the θ direction the control volume is enclosed by the disk surface (as defined above), S_S , and the disk midplane. The two other surfaces that enclose the control volume are marked by S_1 and S_R , and correspond to the vertical arcs at the innermost disk radius ($R = 1$) and at any other radius R . The control volume defined by these surfaces is denoted by $V(R)$.

Thus, the disk mass enclosed by a radius R follows from

$$M(R) = 2 \int_{V(R)} \rho dV, \quad (22)$$

while the mass accretion rate at a certain radius R is

$$\dot{M}_{\text{acc}}(R) = -2 \int_{S_1}^{S_R} \rho \mathbf{V}_p \cdot d\mathbf{S}, \quad (23)$$

and the mass ejection rate is integrated along the disk surface,

$$\dot{M}_{\text{ej}}(R) = -2 \int_{S_S} \rho \mathbf{V}_p \cdot d\mathbf{S}. \quad (24)$$

The mass accretion rate is defined as being positive if it increases the mass in the control volume. The mass ejection rate is defined as being positive if it decreases the mass of the control volume. The factor of two in front of the integrals takes into account the fact that only one hemisphere is treated. Note also a minus sign in front of the integrals.

It is common to introduce the ejection index ξ , which is based on the mass conservation law for a steady solution (Ferreira & Pelletier 1995). It basically measures the steepness of the radial profile of the accretion rate along the midplane. Setting the outer radius to r and the inner radius to unity, the ejection index interrelates ejection and accretion,

$$\frac{\dot{M}_{\text{ej}}}{\dot{M}_{\text{acc}}} = 1 - r^{-\xi}. \quad (25)$$

We obtain the ejection index by a linear approximation of $\xi = -\log(1 - \dot{M}_{\text{ej}}/\dot{M}_{\text{acc}})/\log(r)$ within $r = [2, 10]$. The higher the ejection index, the higher the fraction of accreted matter being ejected within a given radius, and the less matter reaches the inner boundary. For our reference simulation, $\xi \simeq 0.3$ at $T \simeq 10,000$.

Although the disk continuously loses mass (Figure 8), after dynamical times 1000–2000 the disk mass loss is much smaller

than the corresponding ejection and accretion rates. We therefore state that the simulation evolves through a series of quasi-steady states. We find that a continuous disk mass loss is a typical feature of a simulation like our reference simulation. This is because the mass accretion from outside some outer disk radius is not able to sustain the mass that is lost by accretion and ejection within this radius. We also find that the standard diffusivity model typically leads to a magnetic field distribution in the disk that is almost constant in time (not in space). These two facts result in an increase of the disk magnetization in the inner disk, which in turn leads to more rapid accretion in the inner disk.

Figure 8 shows the time evolution of the mass accretion and ejection rates. Note also the general decrease of the mass fluxes over time, which is a direct consequence of the decrease of the disk mass. The behavior and actual values of the mass fluxes are typical in the literature. One should note two distinct features of the mass fluxes. First, the higher integration volume, the higher the mass ejection rate. Second, in jet-launching disks, the mass accretion rate must increase with the radius. These plots also indicate that the evolution of the system can be seen as a consecutive evolution through a series of quasi-steady states.

3.4. Magnetic Field Bending Parameter Study

Here we discuss simulations investigating the influence of the initial magnetic field bending parameter m . We have varied m from 0.2 (strongly inclined) to 0.9 (almost vertical).

Our main result is that although the simulations initially evolve slightly differently, in the long-term they are almost indistinguishable.

Figure 9 shows the time evolution of the ejection to accretion mass flux ratio. The fluxes are again computed for the control volume extending to $R = 10$. It seems to take a few 1000 dynamical time steps for the simulation to lose the memory of the initial magnetic field configuration, but at $t = 10,000$ convergence has obviously been reached. This is also true for the fluxes of angular momentum and energy, and holds as well for the corresponding flux ratios.

The reason why the simulations converge into a single, specific configuration is the fact that it is mainly the diffusivity model that governs the evolution of the magnetic field evolution. When we begin the simulations with the same initial magnetic field strength at the midplane, this results in exactly the same magnetic diffusivity profile. Since we explore rather weak magnetic fields (weaker than the equipartition field), the underlying disk structure cannot be changed substantially by the Lorentz force. On the contrary, the magnetic field distribution adjusts

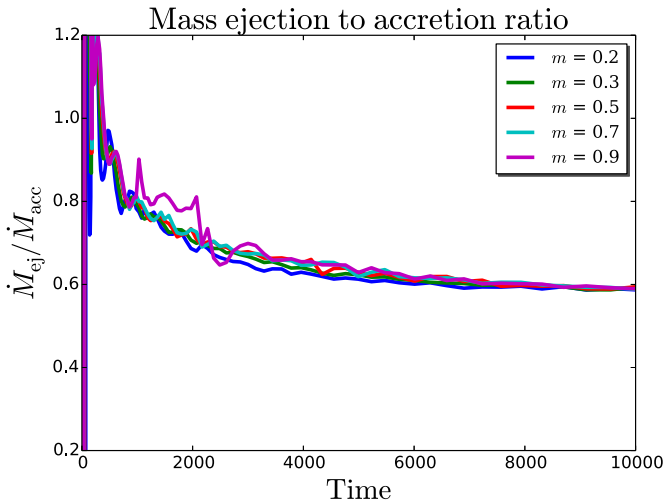


Figure 9. Time evolution of the mass ejection to accretion ratio for simulations evolving from an initial magnetic field distribution with a different initial bending parameter m .

(A color version of this figure is available in the online journal.)

itself in accordance with the diffusivity model, which has the same vertical profile ab initio.

The convergence we observe for these simulations, starting from an initial magnetic field with different bending, again confirms the reliability of our model in general.

3.5. Resolution Study

Here, we briefly present example results of the resolution study. We have performed simulations with a grid resolution of (0.5, 0.75, 1.0, 1.5, 2.0) times our standard resolution of 128 cells per quadrant, corresponding to (64, 96, 128, 192, 256) cells per quadrant, or approximately (8, 12, 16, 24, 32) cells per disk height 2ϵ . Note that once the resolution in the θ direction and the radial extent of the disk is chosen, the resolution in the R direction is uniquely determined (see Section 2.1).

For the resolution study, all simulations were performed up to typically 10,000 time units. Figure 10 shows snapshots of some of these simulations. Essentially, we see an almost identical disk-outflow structure, indicating that numerical convergence has indeed been reached.

Figure 11 shows the time evolution of the mass ejection to accretion ratio, again integrated throughout the control volume

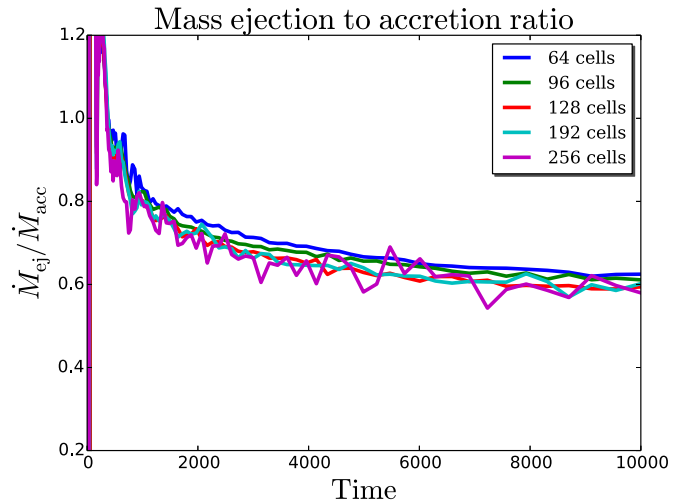


Figure 11. Evolution of the ejection to accretion ratio at $R = 10$ for the reference simulation with different resolutions.

(A color version of this figure is available in the online journal.)

$R < 10$, for simulations of a different resolution. We note two particular issues. First, all curves bunch together at a mass ejection to accretion ratio of about 0.6, indicating convergence of the simulations (this is also true for other flux ratios). Second, the simulation with the highest resolution shows some intermittent behavior (see Figure 10). This might be related to the spatial reconstruction in non-Cartesian coordinates close to the symmetry axis or to the ability to resolve more detailed structures. We conclude that our simulations have converged for the launching region for the resolution chosen.

Note that although the spherical grid is beneficial for a disk and outflow-launching studies, mainly due to the higher resolution of the inner disk, its application to the jet propagation further away from the jet source is limited because of the lack of resolution at larger radii.

4. MAGNETIZATION ANALYSIS

In the following, we investigate a number of physical processes of jet launching by comparing different simulations similar to the reference simulation.

As we have mentioned above, the evolution of our reference simulation can be seen as a sequence of quasi-steady states.

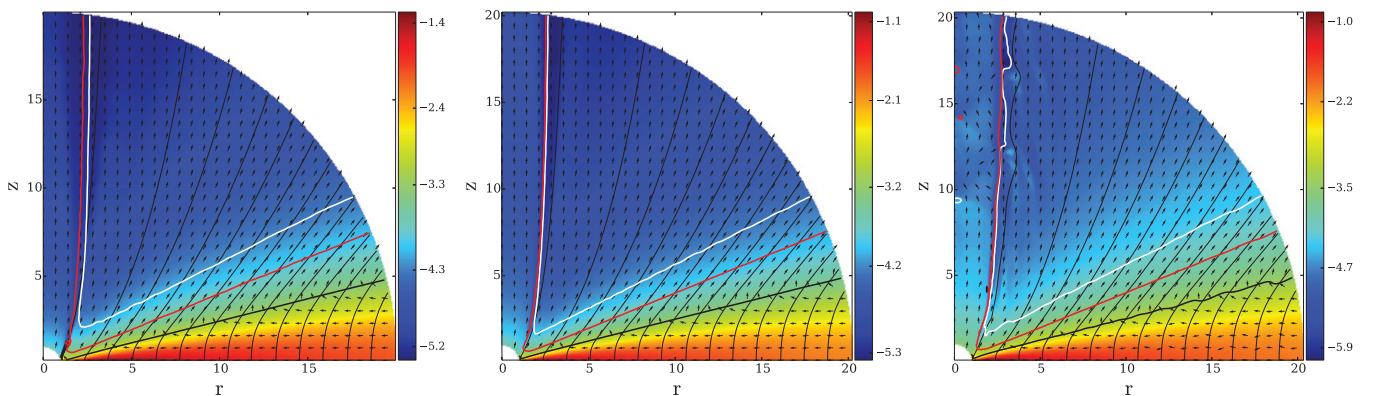


Figure 10. Resolution study. Shown are snapshots of the density distribution at $t = 10,000$ for simulations with different resolutions. From left to right, the resolution is (8, 16, 32) cells per disk height (2ϵ). The black lines mark the magnetic field lines (plotted as flux surfaces). Lines represent the disk (thick black line), the sonic (red line), and the Alfvén (white line) surfaces. Arrows show the normalized velocity vectors.

(A color version of this figure is available in the online journal.)

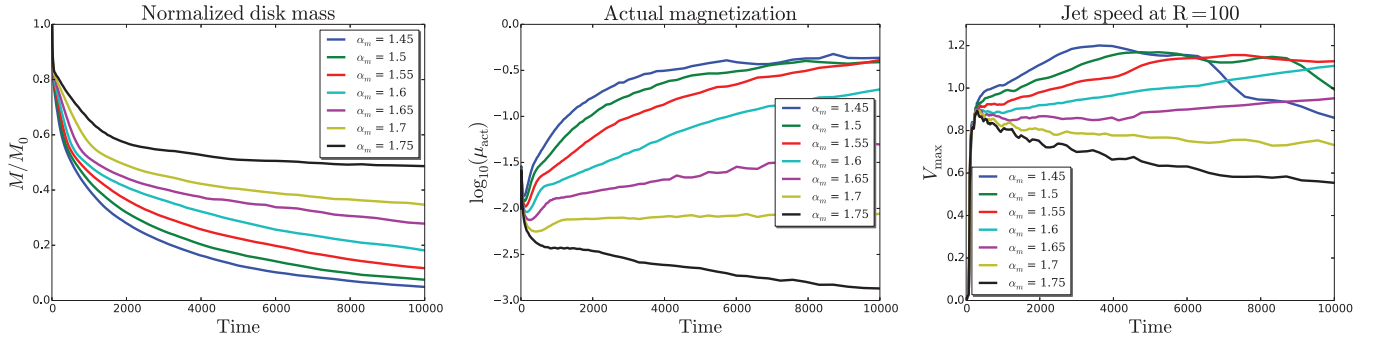


Figure 12. Time evolution of the normalized disk mass (left), the actual magnetization of the disk (middle), and the jet terminal speed (right) for different diffusivity (α_m) strength.

(A color version of this figure is available in the online journal.)

The slow, but constant, decrease of the disk mass eventually leads to a change of the disk magnetization. This is more prominent in the inner part of the disk, whereas the magnetization of the outer disk does not change much. This feature provides the opportunity of studying the disk and jet quantities with respect to the actual disk magnetization.

In this section, we present a set of simulations similar to our reference simulation, however, applying a slightly different choice of parameters. The reference simulation was chosen such that diffusive processes are in balance with advective processes. Now, by choosing a slightly different diffusivity parameter α_m , these processes now are out of balance. This leads either to further faster advection or diffusion of the magnetic field. Naturally, in the case of lower α_m , advection dominates, and, thus, magnetization grows, leading to even faster advection. In the opposite case, the disk magnetization decreases.

This approach allows us to study the evolution of the accretion–ejection in a very general way. Each of the simulations applied has started from the same initial conditions, however, it now follows a different evolutionary track and finally evolves into a quite different state of the system.

Figure 12 shows the time evolution of the disk mass, the average magnetization of the inner disk (averaged between $R = 1.1$ and $R = 1.5$), and the jet speed defined here as

$$V_{jet,act} \equiv \max(V_p)|_{R=100}, \quad (26)$$

the maximum jet speed obtained at $R = 100$, considering only those magnetic field lines rooted in the disk.

We emphasize that the jet speed as computed here is only an extrapolation of the terminal jet speed (at infinity). The general behavior of the disk is as follows. First, the different simulations behave rather similarly. After some time, they begin to differ from each other. At later stages the disks and their outflows arrive at definitely different dynamical states. The exact times at which this happens depends, of course, on the radius for which we examine the disk properties. From Figure 12, we can see that the time when the simulations begin to differ considerably is fairly small, about a few hundred dynamical time steps.

Since we begin the simulation with no accretion, diffusion is not initially in balance. However, electric currents are induced quickly within the disk, and subsequent angular momentum transport results in accretion. Depending on the value of the diffusivity parameter α_m , the system results either in an advection-dominated regime (for $\alpha_m < 1.65$), or a diffusion-dominated regime ($\alpha_m > 1.65$). In principle, an equilibrium situation is possible in which these two processes are in balance. In the case of $\mu_0 = 0.01$, the diffusivity parameter for an equilibrium

situation is around $\alpha_m = 1.65$. We will refer to the critical diffusivity parameter α_{cr} as the one corresponding to the equilibrium state when advection and diffusion are balanced. Generally, the lower the diffusivity, the stronger the advection and thus the resulting magnetization.

We confirm the finding of Tzeferacos et al. (2009) that in the case of a strong magnetic field with $\mu \sim 0.3$, the disk structure changes substantially—the disk becomes much thinner in the inner region of the disk. A stronger magnetic field exerts a stronger torque on the disk, leading to a faster accretion rate. Thus, at some point in time, the accretion velocity becomes supersonic, $M_{R,act} > 1$. We consider this as the limit for applying our magnetic diffusivity model.

As clearly visible from the figures discussed above, for the present setup the current diffusivity model (Equation (14)) is only marginally stable—all deviations from the critical diffusivity will be further amplified. If magnetic diffusion dominates the disk, the magnetic field becomes increasingly weaker unless at about $\mu \sim 0.001$, where the jet outflow can no longer be sustained. On the other hand, a weaker diffusivity leads to a faster accretion that also results in a runaway process. One way to circumvent this problem is to apply a different model for the diffusivity, namely $\alpha_{ssm}(\mu)$ (see Section 5).

As might be easily seen from Figure 12, ongoing disk mass depletion in most cases leads to a higher degree of disk magnetization, a process that happens faster for less diffusive, thus higher, advective simulations. A change in magnetization may substantially change the dynamics of the disk. Stronger magnetization, for example, leads to a higher jet speed.

One might notice the deviation in the behavior of the jet terminal speed for a low value of α_m . We believe that this results from the position where we calculate the terminal speed—for this case the jet accelerates even further out and the asymptotic velocity is not reached at $R = 100$ for the low α_m (or highly magnetized) case and is still in the process of transforming the magnetic energy into kinetic. In a follow up paper, we will discuss the terminal jet speed much more detail, demonstrating that for a moderately weak magnetic field, $\mu \approx 0.05$, the terminal jet speed already reaches unity.

In summary, we state that it is the actual magnetization in the disk that governs ejection and accretion and that is directly linked to various disk–jet quantities.

4.1. Transport of Angular Momentum and Energy

Here we present the analysis of the angular momentum and energy transport in our simulations. It is common to explore the angular momentum and energy transport by means of their

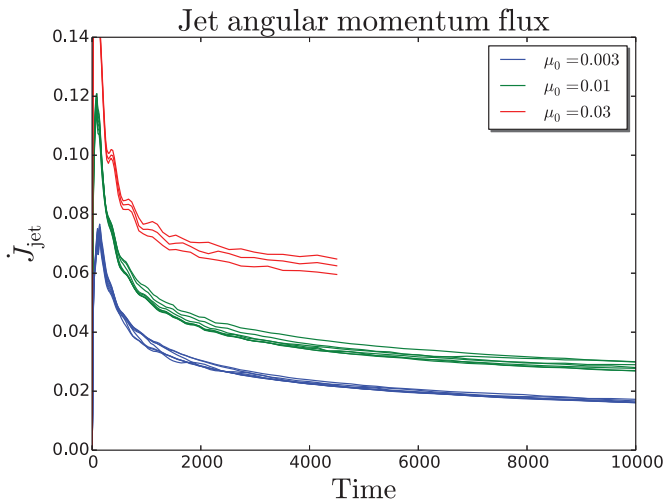


Figure 13. Time evolution of the jet angular momentum flux for the reference simulation at radius 10. Simulations with different initial magnetic fields form three distinct groups corresponding to $\mu_0 = (0.003, 0.01, 0.03)$ (from bottom to top).

(A color version of this figure is available in the online journal.)

fluxes through a control volume. We define the accretion angular momentum flux $\dot{J}_{\text{acc}} = \dot{J}_{\text{acc,kin}} + \dot{J}_{\text{acc,mag}}$ as the sum of the kinetic and magnetic parts, keeping the same control volume as for the mass fluxes (see Appendix B).

Figure 13 shows the time evolution of the jet angular momentum flux for a number of simulations. We divide them into three different groups distinguished by their initial magnetization, $\mu_0 = 0.003, 0.01, 0.03$. Different lines within each group represent simulations with different diffusivity parameters α_m . The jet angular momentum flux is calculated through the upper part of the control volume, thus, up to $R = 10$.

As expected, the stronger the overall magnetic field strength is in the disk, the stronger torque it exerts, and thus the higher angular momentum fluxes we find.

Although the magnetic diffusivity parameter α_m differs within each group of lines (marked by different colors), the total torque measured for the corresponding simulations is about the same. This comes from the fact that the total torque is set by the global magnetic field. Thus, the evolution of the total torque is mainly set by the initial conditions.

We note that the simulations applying a strong initial magnetic field (represented by the upper bundle of curves in Figure 13) have been interrupted earlier compared to usual evolution times. For these cases, the inner part of the disk became highly magnetized. The strong magnetic field changes the inner disk structure such that our model for the magnetic diffusivity can no longer be applied. This is simply because the actual scale height of the disk significantly decreases and no longer coincides with the initial disk surface. We consider the case of strong magnetic fields as being beyond the scope of this paper. The underlying turbulence might be significantly suppressed as well.

In accordance with previous works (see, e.g., Zanni et al. 2007), we find that the ratio of angular momentum extracted by the jet to that provided by the disk accretion is always close to, but slightly larger than, unity, $\dot{J}_{\text{jet}}/\dot{J}_{\text{acc}} \gtrsim 1$. The main reason is that the accretion rate in the outer part of the disk is too low to compete with a strong mass loss by the disk wind at these radii.

We define the accretion energy flux (accretion power) as the sum of the mechanical (kinetic and gravitational), magnetic, and

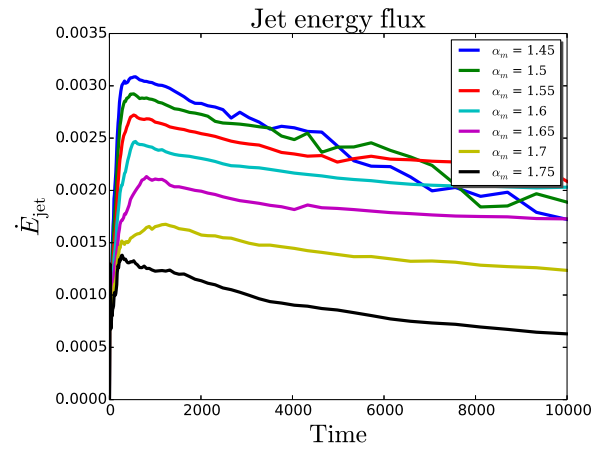


Figure 14. Time evolution of the jet energy flux for the reference simulations at radius 10.

(A color version of this figure is available in the online journal.)

thermal energy fluxes,

$$\dot{E}_{\text{acc}} = \dot{E}_{\text{acc,kin}} + \dot{E}_{\text{acc,grv}} + \dot{E}_{\text{acc,mag}} + \dot{E}_{\text{acc,thm}},$$

and, similarly, the jet energy flux (jet power) by

$$\dot{E}_{\text{jet}} = \dot{E}_{\text{jet,kin}} + \dot{E}_{\text{jet,grv}} + \dot{E}_{\text{jet,mag}} + \dot{E}_{\text{jet,thm}}.$$

In contrast to the angular momentum flux, most of the energy flux is being released from the inner part of the disk. This makes the energy flux very sensitive to the conditions in the inner disk. Indeed, Figure 14 shows that the power liberated by the jet strongly depends on the diffusivity parameter, which is the main agent for governing the magnetic field strength. A weaker diffusivity parameter α_m leads to a higher magnetization, and thus a higher jet power. The same is true for the accretion power.

We further find that the ratio of energy fluxes, namely the ratio of the jet to the accretion energy flux, is always close to, but slightly lower than, unity. This is also in accordance with Zanni et al. (2007).

In this section, we have provided some evidence that it is the actual magnetization in the disk that governs the fluxes of mass, energy, and angular momentum. In the next section, we show how exactly these fluxes are connected to magnetization.

4.2. Analysis of Magnetization, Diffusivity, and Fluxes

In a steady state, diffusion and advection balance. Advection of the magnetic flux in principle increases the magnetic field strength, predominantly in the inner disk. On the contrary, the diffusion smooths out the magnetic field gradient. Therefore, the diffusivity model applied is a key ingredient for these processes, directly influencing the disk structure and evolution.

In the following analysis, we will not focus on the profile or the magnitude of the magnetic diffusivity, but concentrate on the resulting magnetization and its time evolution. As discussed above, by changing the magnetic diffusivity parameter α_m , we are able to explore how the actual disk magnetization influences various properties of the disk–jet system.

For each parameter run performed, we measure the actual physical variables in the disk–jet system, such as the time-dependent mean magnetization, accretion fluxes, jet fluxes, or the accretion Mach number. Naturally, the actual value of a certain property has evolved from the initial value during the

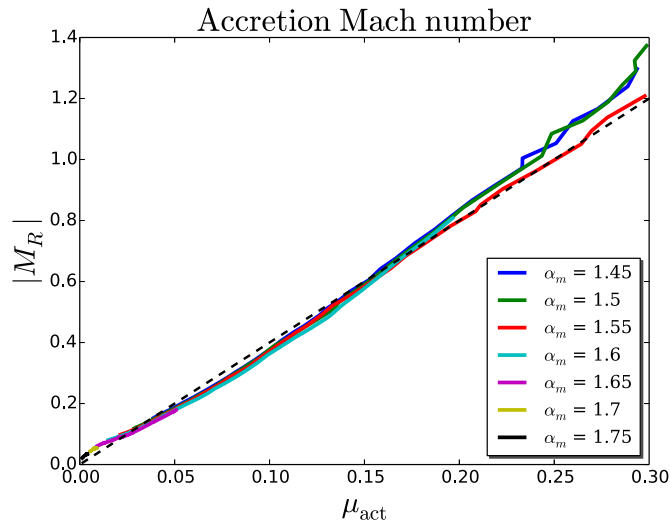


Figure 15. Relation of the accretion Mach number to the actual magnetization for the initial magnetization $\mu_0 = 0.01$. The linear approximation $M_R = 4\mu$ is shown by the dashed black line.

(A color version of this figure is available in the online journal.)

simulation. With a mean value we denote the values averaged over a small area of the inner disk,

$$X \equiv \langle X(r, z = 0) \rangle. \quad (27)$$

All mean quantities discussed are averaged over the inner disk midplane from $R = 1.1$ to $R = 1.5$. The choice of the averaging area is motivated as follows. First, in order to avoid any influence of the inner accretion boundary we have moved the inner integration radius about 10 grid cells away from it. Second, we are interested in examining the inner part of the disk, since it is the region where the magnetization is changing predominantly and it is the launching area for the most energetic part of the jet. Third, we want to avoid large magnetic gradients affecting our averaging area. Although most of jet energy is launched from regions broader than this small area, the area is seen as representative. We emphasize that the profiles of the jet power along the disk surface are similar for all simulations. In all cases we investigated, we find that the general behavior of the physical outflow or disk quantities with respect to underlying disk magnetization does not depend on the area where the averaging is performed (on neither the location nor the size).

Keeping all other parameters the same, we have carried out simulations varying the initial magnetization μ_0 and the strength of the magnetic diffusivity α_m . For all our simulations, starting with different initial magnetization, $\mu_0 = 0.003$, $\mu_0 = 0.01$, and $\mu_0 = 0.03$, we find that the interrelation between the different jet or disk quantities and the disk magnetization is essentially the same. We therefore present only one group of simulations, namely that with $\mu_0 = 0.01$. Although the initial magnetic field strength differs, we can already suspect at this point that it is the actual rather than the initial strength of the magnetic field in the disk that governs the disk accretion and ejection of the jet, and thus plays a major role in the launching process. This has not yet been discussed in the literature, as most publications parameterize their simulations by the initial parameters. An exception might be Sheikheezami et al. (2012), who pointed out substantial changes in the disk plasma beta during the time evolution.

An interesting representation of the evolution of the main disk-jet quantities are (μ, X) plots, where X stands for the examining variable. Note that in these plots the time evolution is hidden.

4.2.1. Accretion Mach Number

As was shown by Königl & Salmeron (2011), there is a link between the mean accretion Mach number and the disk magnetization. In our terms, this relation can be expressed as

$$M_{R,\text{act}} = \frac{2}{\sqrt{\gamma}} q \mu_{\text{act}}, \quad (28)$$

where q is the magnetic shear,

$$q = \frac{H J_R}{B_p} = -\frac{B_\phi^+}{B_p}, \quad (29)$$

and where the plus sign denotes a variable estimated on the disk surface. Note that in our case there is no viscous contribution and the factor $1/\sqrt{\gamma}$ appears in the relation since the accretion Mach number is calculated using adiabatic sound speed.

Figure 15 shows that setting q to constant $q = 2\sqrt{\gamma}$ (thus $M_R = 4\mu$) is a good first approximation, especially for the strong magnetization cases. As we will see in the next section, in the case of a weak magnetic field, the magnetic shear q behaves far from being constant. Closer examination of the magnetic shear q reveals a presence of two different jet launching regimes.

4.2.2. Magnetic Shear

A tight relation exists between the magnetic shear q and the ratio between the toroidal and poloidal magnetic field components. We define the magnetic shear q by the radial electric current at the disk midplane, since it does not require us to apply the notation of the disk surface, which, in case of a strong magnetic field, might change by up to 40%. Note that the magnetic shear is the first derivative of the accretion Mach number with respect to the magnetization. Therefore, it shows the growth rate of the local Mach number or steepness of the curve.

Figure 16 shows the magnetic shear with respect to the underlying inner disk magnetization. We see that the magnetic shear behaves in two different ways—in the case of low magnetization, $\mu \leq 0.03$ – 0.05 , the magnetic shear is substantially higher in comparison to the case of high magnetization, $\mu \geq 0.03$ – 0.05 . The explanation is straightforward: there is a turning point concerning the generation of the toroidal magnetic field versus flux losses through the disk surface (by the outflow). To understand this, one needs to set apart the generation processes of the toroidal magnetic field from the loss processes. The rate of the generation of the magnetic field in Keplerian disks is primarily set by the structure of the magnetic field and is rather constant in the case of a quasi-steady state. On the other hand, the outflow speed (through the disk surface) is highly dependent on the actual disk magnetization. In the case of a weak magnetization, the outflow speed is rather small, which makes it possible to sustain a stronger magnetic shear. A strong disk magnetization results in a fast outflow, thus setting the maximum limit for the magnetic shear.

4.2.3. Mass and Energy Flux

The magnetic shear has a great impact on outflow launching (Ferreira & Pelletier 1995). We confirm this finding by presenting the mass and energy ejection and accretion fluxes.

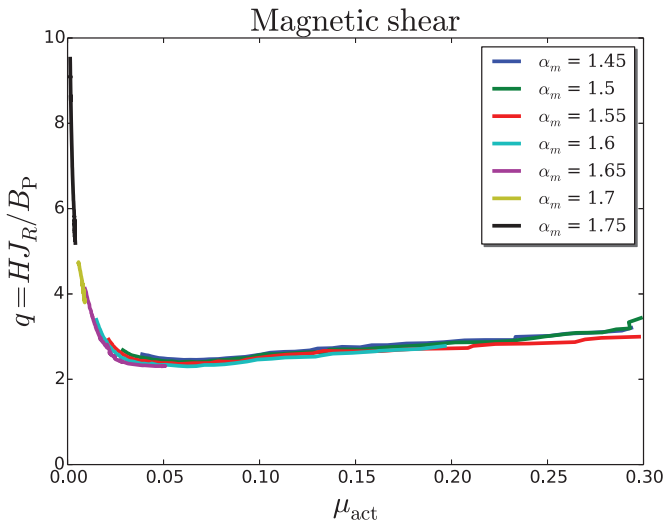


Figure 16. Relation of the magnetic shear with respect to the actual magnetization.

(A color version of this figure is available in the online journal.)

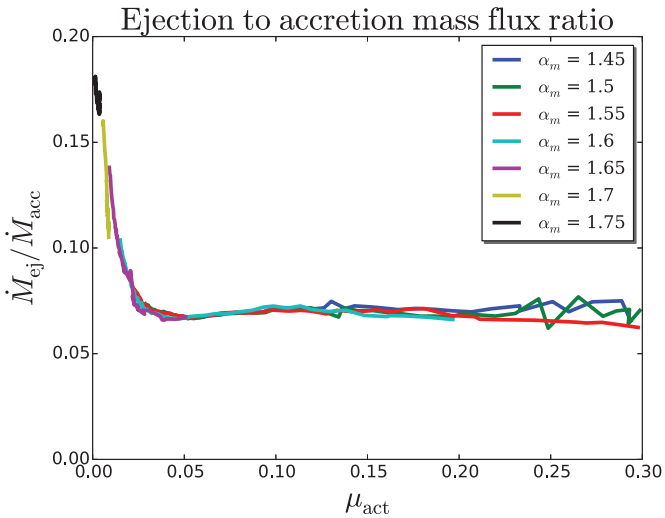


Figure 17. Relation of the mass ejection to accretion ratio with respect to the actual magnetization.

(A color version of this figure is available in the online journal.)

Figure 17 shows the ratio of the mass ejection rate, $\dot{M}_{\text{ej}}(1.5) - \dot{M}_{\text{ej}}(1.1)$, to the accretion rate, both averaged over the same area. Obviously, the ejection efficiency is higher for weaker magnetized disks.

This is easy to understand considering Equation (21). In the case of a weak magnetic field, the strong magnetic shear (the high toroidal to poloidal magnetic field ratio) leads to faster poloidal acceleration, which is caused by the force component parallel to the magnetic field. This force also extracts the matter from the disk. In the case of a strong disk magnetization, the acceleration of matter is primarily supported by the centrifugal force.

We note that studying the ejection index (calculated within an area $R = 2 \dots 10$) with respect to the mean disk magnetization leads to very similar results, that is a saturation to values of about 0.35–0.40 in the case of high magnetization and a significant increase in the case of low magnetization.

Figure 18 shows the ratio of the energy ejection density to the average accretion energy, computed in the same way as for

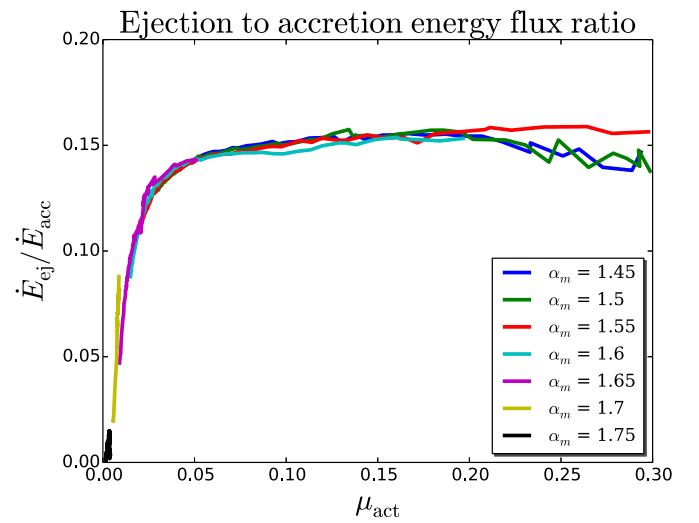


Figure 18. Relation of the energy ejection to accretion with respect to the actual magnetization.

(A color version of this figure is available in the online journal.)

the mass fluxes. Compared to the mass fluxes, the energies show opposite behavior—the ejection to accretion power is an increasing function with magnetization. This is a highly important relation, since it relates two observables. Note that following our findings, there is not a fixed value for the ratio between the jet and accretion power. This should be considered when comparing observational results to theory.

Essentially, this result shows the general importance of the magnetic energy flux compared to the mechanical energy. The mechanical energy flux is always negative, while the magnetic energy flux is positive. In the case of a strong magnetic field, our results are similar to Zanni et al. (2007), namely, that magnetic energy flux dominates the mechanical flux. We also see a saturation of the flux ratio in the case of a moderately strong magnetization. We find that in a weak magnetization case the energy flux ratio can be very small.

We also find that the ejection Mach number, Equation (19), increases almost linearly with magnetization.

Essentially, the general behavior of the mass and energy flux ratios does depend on the averaging area or its position.

The accretion power (see Appendix B, Equation (B3)) is mainly determined by the accretion rate at the inner disk radius. Assuming a typical scale height for the mass accretion as ϵr , the accretion power can be estimated considering the magnetic shear and the actual magnetization of the disk,

$$\dot{E}_{\text{acc}} \simeq 0.06 q \mu_{\text{act}} \dot{E}_0, \quad (30)$$

where \dot{E}_0 is the unit power (see Appendix A).

In the case of strongly magnetized disks, one can assume that the magnetic shear is approximately constant $q \approx 3$, and this relation transforms into $\dot{E}_{\text{acc}} \simeq 0.2 \mu_{\text{act}} \dot{E}_0$. Note that this result connects two essential quantities—the accretion power, which manifests itself by the accretion luminosity, to the disk magnetization, which is intrinsically hidden from the observations.

5. A STABLE LONG-TERM EVOLUTION

In this section, we discuss the commonly used diffusivity model and the reasons why we believe that it fails in the case of very long-term simulations, in particular when treating weakly

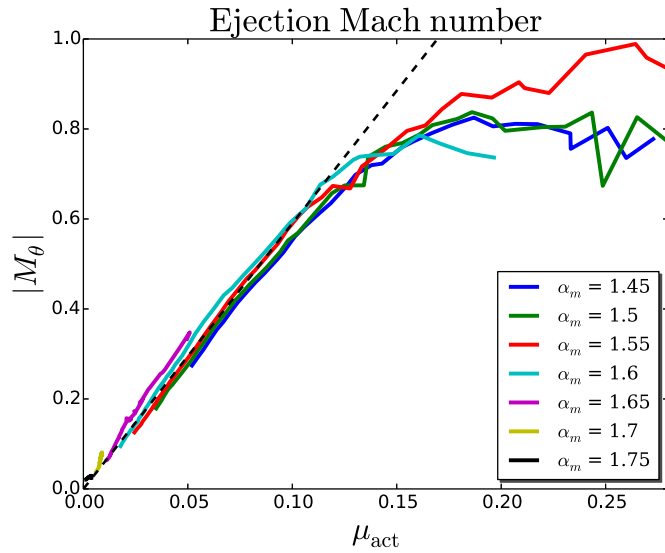


Figure 19. Relation of the ejection Mach number with respect to actual magnetization. The slope of the dashed line is $\beta = 5.9$.

(A color version of this figure is available in the online journal.)

magnetized disks. In order to overcome this problem—the accretion instability—we propose another magnetic diffusivity model. This new model enables us to simulate the evolution of the disk–jet system for much longer times.

5.1. Constraints on the Diffusivity Parameters

The simple idea that the induction of the magnetic flux in steady state is compensated by the flux losses, both by diffusion and magnetic flux escape through the disk surface, becomes barely applicable in the case of a weak magnetic field. As discussed previously (see Section 2.5), in order to keep the magnetic field distribution properly bent, the magnetic diffusivity parameter α_m must be linked to the anisotropy parameter χ . Equation (20) was obtained considering the standard magnetic diffusivity model. A more general relation can be derived assuming a curvature of the magnetic field of about 0.5, which is the mean curvature of the initial field distribution (see Equation (9)),

$$(\alpha_{\text{ssm}}\chi - M_\theta)\alpha_{\text{ssm}} \leq \mu. \quad (31)$$

Solving this inequality for α_{ssm} and assuming $M_\theta \propto \beta\mu$, we find

$$\alpha_{\text{ssm}} \leq \alpha_0 = \frac{\beta}{2}\mu_\chi + \sqrt{\left(\frac{\beta}{2}\right)^2 \mu_\chi^2 + \mu_\chi}, \quad (32)$$

where $\mu_\chi = \mu/\chi$, and $\beta \approx 6$ in our simulations. This relation shows that in order to keep the disk magnetic field properly bent, the α_{ssm} should behave differently in the two limits of magnetization: a linear relation to the magnetization in the case of a strong magnetic field, and proportional to the square root of magnetization in the case of a weak field. In the case of a strong deviation from this relation, the magnetic field structure will be substantially affected, resulting in a high field inclination (for $\alpha_{\text{ssm}} \ll \alpha_0$), or a strong outward bending (for $\alpha_{\text{ssm}} \gg \alpha_0$).

For Equation (32), we have implicitly assumed a linear relation between the ejection Mach number (at the disk surface) and the magnetization. In fact, our simulations approve such an interrelation. Figure 19 shows that for a moderately strong magnetic field, there is a linear relation between the ejection

Mach number and the underlying disk magnetization. This behavior is also consistent with the ejection to accretion mass flux ratio we have discussed above.

As a consequence of Equation (16), the α_{ssm} plays a direct role in determining the strength of the poloidal electric current with respect to the toroidal current. We find in our simulations that in order to sustain jets, the ratio of the poloidal to the toroidal current should be sufficiently high (about 15).

The difficulty in performing simulations of weakly magnetized outflows is that the specific torques may increase toward the disk surface area due to the low densities in that area. This will lead to a layered accretion along the disk surface, and thus much lower accretion along the midplane. Although this might be a relevant process in reality, our numerical setup is not suited for the treatment of such a configuration.

The standard, commonly used magnetic diffusivity model is parameterized by two constants, α_m and χ . In general, choosing a high anisotropy parameter χ implies a low diffusivity parameter α_m . Together, this will lead to a decrease in the poloidal electric current and an increase in the toroidal current (see Equation (16)). Thus, the resulting torque will not be sufficient to brake the dense matter along the midplane, and will lead to layered accretion. An anisotropy parameter lower than unity has proven to lead to a smoother time evolution, since it allows for stronger poloidal currents at the midplane, and thus a mass accretion that is developed over the full disk height. Another option to have $\chi > 1$ would be to modify the vertical diffusivity profile such that it reaches the maximum not at the disk midplane, but at the disk surface. This would also help to develop a strong electric current in the disk midplane.

5.2. The Accretion Instability

Here, we discuss another problem, which is common in the standard diffusivity model. As previously shown, most of the simulations suffer from the mass loss from the disk, leading to the increase of magnetization. However, the increase of magnetization further amplifies the mass loss. This is known as the accretion instability, first studied by Lubow et al. (1994), and later confirmed for more general cases (Campbell 2009). If, on the other hand, the diffusivity is too high (chosen by a high α_m parameter), the inevitable diffusion of the magnetic field will lead to the situation where a jet can no longer be sustained.

We emphasize that the main reason for the increase in magnetization is the mass loss, but not the actual magnetic field amplification. This is a direct consequence of the accretion instability, namely, a lack of sufficient feedback that could bring the accretion system back to a stable state. In other words, in order to run long-term simulations, one needs to apply a diffusivity model that provides a stronger feedback to the diffusivity profile than the standard choice $\propto \sqrt{2\mu}$.

5.3. A Proper Magnetization Profile

The direct consequence of the accretion instability is that the magnetization increases toward the center. It is easy to show that the behavior of the magnetization has to be opposite. In accretion disks producing outflows, the mass accretion rate must naturally increase with radius. Assuming a radial self-similarity of the disk and taking into account that the accretion Mach number is linearly related to the magnetization and that $\rho \propto C_s^3$, one derives

$$\beta_\mu = \xi - 2 - 4\beta_{C_s}, \quad (33)$$

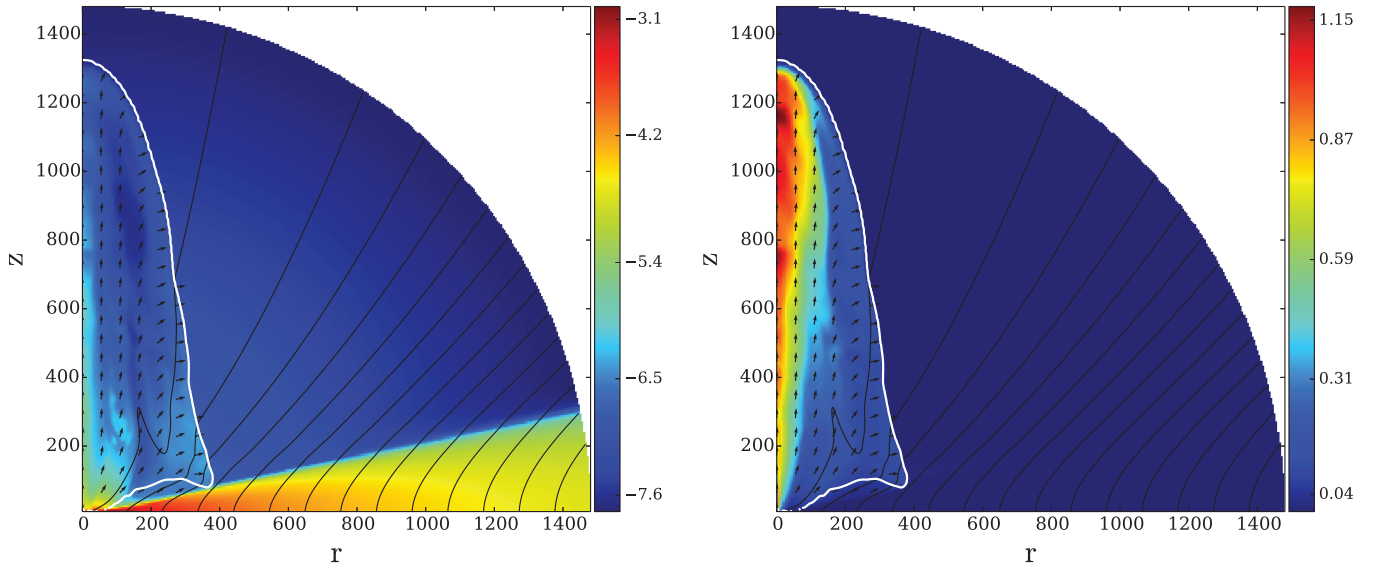


Figure 20. Initial evolution of the strong diffusivity setup at $T = 1500$. The colors represent the logarithm of density (left) and speed (right), the black lines denote the magnetic field, the arrows denote the normalized velocity, and the white line shows the Alfvén surface. Arrows show normalized velocity vectors.

(A color version of this figure is available in the online journal.)

where ξ is the ejection index and β_X represent the power-law index of a physical quantity X . Considering that magnetized disks are very efficient in producing outflows, $\xi \approx 0.2\text{--}0.4$, one may expect β_μ to be positive (if $\beta_{C_s} \approx -1/2$), thus, an increasing function with radius. However, the disk structure itself can be re-arranged such that $|\beta_{C_s}| \leq 1/2$, which eventually will satisfy the relation 33. This is indeed what we find.

One should, however, keep in mind that this equation is a rough estimate and might be subject to the different disk physics involved. If the magnetic torque is not the only supporter of the accretion, as in the case of the viscous simulations of Murphy et al. (2010), the above presented relation might be relaxed. However, similar analysis can be performed to set the limit of the magnetization with respect to other quantities.

5.4. A Modified Diffusivity Model

In this section, we present a diffusivity model, which does not suffer from the accretion instability. Although the standard diffusivity model gave us the opportunity to probe a wider parameter space, it is not applicable for very long-term studies.

We emphasize that the transition from the a direct simulation of turbulence to the mean field approach, which lacks the small scales by design, is indeed subtle. So far, in the literature, the jet launching problem is addressed without considering the origin of the magnetic field by a dynamo. Therefore, the only way of amplifying the magnetic field is by advection (or stretching in case of a toroidal field). There is also no intrinsic angular momentum transport by the turbulence itself. The only term we need to model when applying a small-scale turbulence is the effective magnetic diffusivity. This might have surprising consequences. In order to suppress the turbulence, one should rather amplify the effective diffusivity—leading to a stronger decay of the magnetic field and resembling the quenching of diffusivity (or dynamo)—rather than decrease it, leading to stronger advection and thus an amplification of the magnetic field. The main motivation of our new model for the diffusivity is to consider stronger feedback by the disk magnetization. We overcome the accretion instability by assuming a stronger

dependence of α_{ssm} on the magnetization,

$$\alpha_{\text{ssm}} = \alpha_m \sqrt{2\mu_0} \left(\frac{\mu}{\mu_0} \right)^2, \quad (34)$$

where we choose $\alpha_m = 1.55$ and $\mu_0 = 0.01$. Here we keep the previous overall form and constants, indicating that both models are the same at the magnetization μ_0 . A quadratic dependence on μ was chosen in order to amplify the feedback. Choosing a power lower than two might have revealed other complications, for example, feedback too weak to work fast enough, and keep α_{ssm} under the constraint of Equation (32). We will refer to this diffusivity model as the strong diffusivity model.

5.5. The Long-term Disk-outflow Evolution

Applying our strong diffusivity model enables us to overcome the accretion instability. As a result, we were able to perform our simulations for much longer times, reaching evolutionary time steps of $t > 150,000$, which corresponds to approximately 25,000 revolutions at the inner disk orbit.

Figure 20 shows the typical computation domain and the initial dynamics of the system. As usual, the evolution starts with the propagation of the toroidal Alfvén wave, resulting in a propagating cocoon. At this point, the innermost area ($R \leq 10$) has reached a quasi-steady state, while the outer part has not even slightly moved from the initial state. Figure 21 presents the same simulation at a later state when a strong outflow has been developed. Notice the difference between the inner part, $r \leq 200$, and the outer part, $r \geq 200$. The inner part has already relaxed to a steady state, while the outer region shows rapid accretion and ejection patterns. This is a direct consequence of the new diffusivity model. The logic behind implementing the enhanced feedback is valid only when the accumulation of the flux is possible. The initial imbalance between advection and diffusion in the outer part leads to a rapid advection of the magnetic flux to the inner disk. As a result, the rapid accretion further leads to higher inclination angles of the magnetic field (smaller angle with respect to the disk surface). This results in a higher efficiency for the toroidal magnetic field induction, thus leading to even more rapid accretion and ejection.

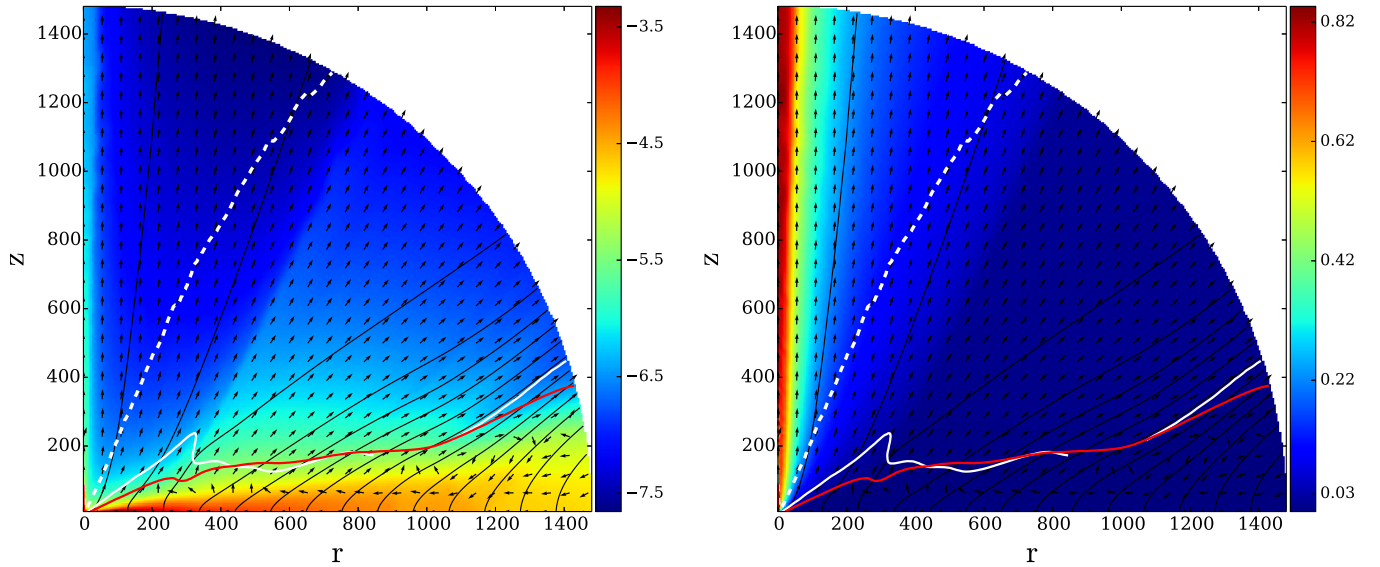


Figure 21. Time snapshot of the strong diffusivity setup at $T = 150,000$. Shown are the density (colors, in logarithmic scale), the poloidal magnetic flux (thin black lines), the sonic (red line), the Alfvén (white line), and the fast magnetosonic (white dashed line) surfaces. Arrows show normalized velocity vectors.

(A color version of this figure is available in the online journal.)

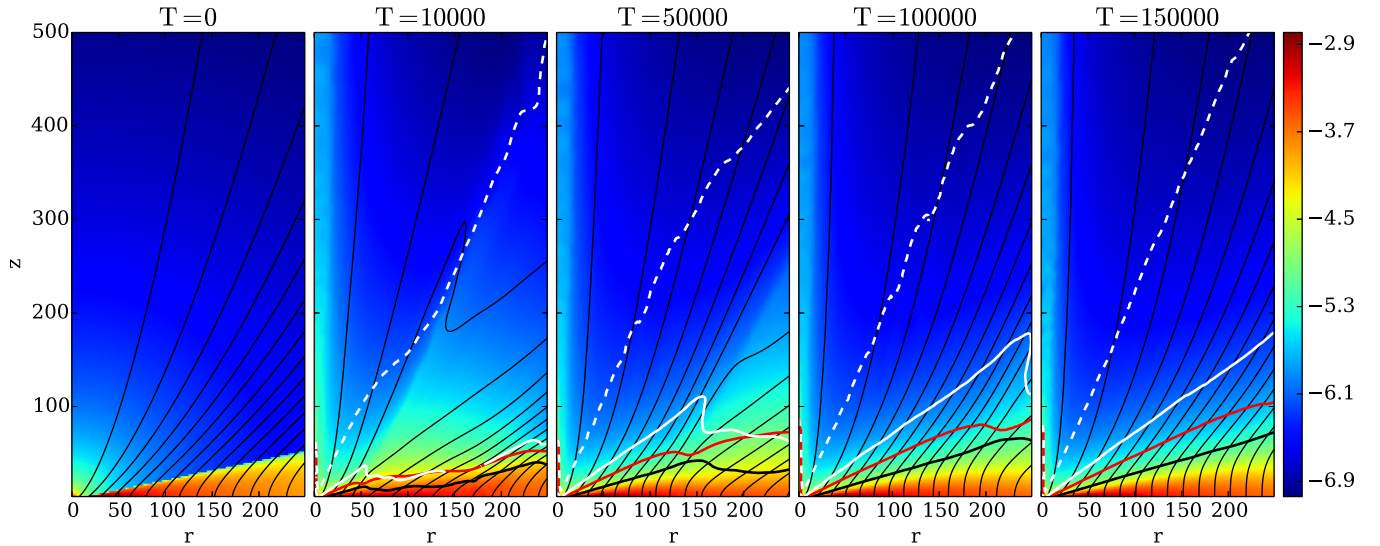


Figure 22. Time evolution of the disk-jet structure for the strong diffusivity simulation. Shown is the evolution of density (colors, in logarithmic scale), the poloidal magnetic flux (thin black lines), the disk surface (thick black line) the sonic (red line), the Alfvén (white line), and the fast magnetosonic (white dashed line) surfaces.

(A color version of this figure is available in the online journal.)

Figure 22 shows the long-term evolution on a small sub-grid of the simulation with our strong diffusivity model. As can be seen, until time $t = 10,000$, only a small fraction of the disk has dynamically evolved (up to $R \approx 50$), while at later times the outer parts of the disk also reach a new dynamic state. A steady outflow is established from the whole disk surface (shown on this sub-grid) and reaches a super-fast magnetosonic speed. Note that the positions of the critical MHD surfaces are constant in time, which is a further signature of a steady state.

The outflow reaches maximum velocities typically of the order of 100 km s^{-1} for YSO, or $70,000 \text{ km s}^{-1}$ in case of AGNs. Concerning observationally relevant scales, our simulations compare to the following numbers. Our numerical grid is comparable to 150 AU for YSO, and 0.14 pc in the case of AGNs. Physically more meaningful is the grid size where our simulation has reached a steady state. This is a size comparable to 25 AU for YSO, and 5000 AU in the case of AGNs, but can be extended

by running the simulations longer. The dynamical timescale of 150,000 time units (or 25,000 disk orbits) corresponds to about 550 years in the case of YSO and about 200 years in the case of AGNs. Typical accretion rates of our simulations are $3 \times 10^{-7} M_{\odot} \text{ yr}^{-1}$ for YSO and $0.1 M_{\odot} \text{ yr}^{-1}$ in the case of AGNs, but one has to keep in mind that these values depend not only on the intrinsic scaling of the central mass and inner disk radius, but also on the scaling of density. Therefore, we herewith present the most extended and longest MHD simulations of jet launching obtained so far—connecting the jet launching area close to the central object with the asymptotic domain, which is accessible by observations.

Although a spherical grid is computationally very efficient and may allow us to extend the computational domain to almost any radius, in reality its application for the jet-launching simulations is somewhat limited. There are two reasons for that. First, it takes obviously much longer time for the outer disk

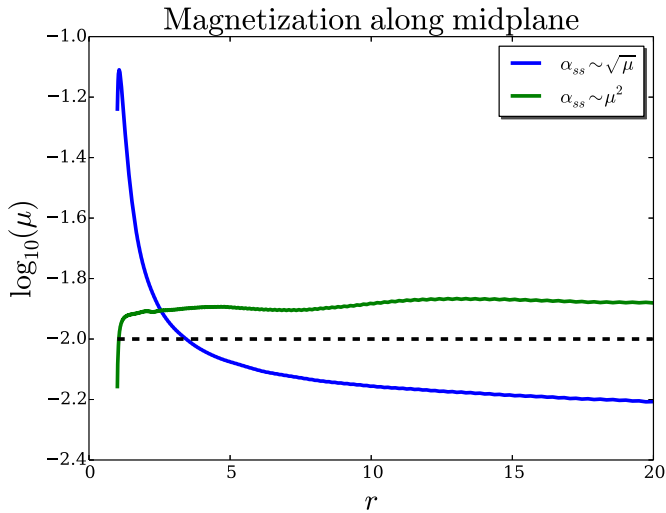


Figure 23. Magnetization distribution throughout the disk for reference and the strong diffusivity model at $T = 10,000$. The dashed line marks the initial magnetization.

(A color version of this figure is available in the online journal.)

areas to evolve into a new dynamical steady state. Thus, the outer disk will remain close to the initial state of the simulation for quite some time. Second, a more severe drawback is the lack of resolution for the asymptotic jet. For example, for distances $R > 500R_0$ along the rotational axis, a jet radius of about $r_{\text{jet}} \approx 25$ can be resolved only by about five grid cells (applying our typical resolution). We therefore restrict our computational domain for such grid size to about $R_{\text{out}} \simeq 1000\text{--}2000R_0$. The above-mentioned resolution issue is in fact one of the advantages for using cylindrical coordinates for jet formation simulations.

5.6. Results of the Strong Diffusivity Model

By design, the purpose of our strong diffusivity model was to avoid the accretion instability. As a consequence of this application, the magnetization profile does not decrease with radius (see Figure 23). Although both simulations (with standard and strong diffusivity model) start from the same initial disk magnetization, the disk evolution results in a quite different magnetization distribution. The standard diffusivity model (our reference simulation from above) results in a magnetization profile decreasing with radius. In contrast, for the strong diffusivity model, a rather flat magnetization profile emerges. In non-viscous simulations, assuming radial self-similarity, a flat (or not decreasing with radius) profile is essential for sustaining a continuous accretion flow at any given radius.

As soon as a steady state is reached, the evolutionary track for this simulation is represented by a simple dot in all (μ, X) diagrams (at least from 1000 to 150,000 time units). The mean inner disk magnetization is $\mu \approx 0.012$. We find that this simulation fits to every relation presented above, such as mass and energy flux ratios, or magnetic shear, that were derived applying a standard diffusivity model. In other words, the aforementioned dots belong to the curves drawn in the (μ, X) diagrams.

There are several distinct features one can derive from the resulting magnetic field structure. Figure 24 shows the toroidal to poloidal magnetic field component ratio. Taking into account that the disk magnetization (calculated from poloidal component only) is uniform, three different regions can be distinguished. The first region is between the midplane and the disk surface

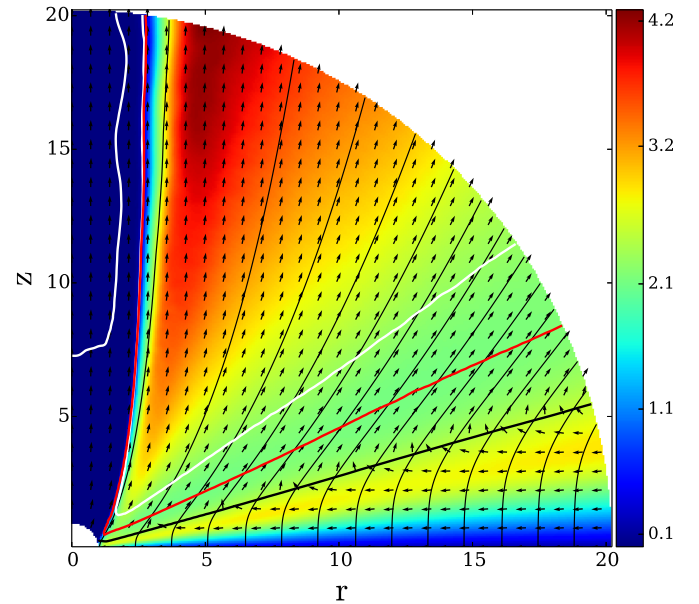


Figure 24. Ratio of the toroidal to poloidal magnetic field for the strong diffusivity model at $T = 10,000$. The lines represent the disk (thick black line), the sonic (red line), and the Alfvén (white line) surfaces. Arrows show normalized velocity vectors.

(A color version of this figure is available in the online journal.)

where the toroidal magnetic field reaches its maximum and the torques change sign. The second region is between the disk surface and the Alfvén surface where the ratio of the field components is quite constant. The third region is beyond the Alfvén surface when the poloidal component of the magnetic field becomes weak enough to keep a rigid magnetic field structure and the toroidal component starts to dominate the poloidal one.

5.7. Dynamical Profiles of a Steady State Accretion Disk

In this subsection, we further explore the disk structure in a steady state. In Figure 25, we present the radial profiles of certain magnetohydrodynamical variables along the midplane. We show the profiles derived from our numerical simulations with their approximations by power laws, and compare them to the initial distribution. These radial profiles are obtained along the disk midplane, however, they also hold for at least one disk semi-height. The thetoidal profiles that normalized to the corresponding midplane value (not shown here) almost coincide with each other, indicating that the assumption of a self-similar disk is in fact reasonable, though different power indexes should be used.

In particular, Figure 25 shows how the disk structure evolves from a certain initial power-law distribution into another power-law profile. We see distinct power-law profiles for radii up to $R \leq 250$. This corresponds to the area where the disk evolution has reached a steady state. For very small radii, $R \leq 1.1$, we also see a deviation from a power-law profile, which we consider as a boundary effect.

At time $t = 150,000$, we find the following numerical values for the power-law coefficients β_X for the different variables at the midplane $X(r, \theta = \pi/2) \sim r^{\beta_X}$. The disk rotation remains Keplerian throughout the entire evolution, thus $\beta_{v_\phi} = -1/2$. The radial profiles for density and gas pressure slightly change from their initial distribution. The density power-law index changes from $\beta_\rho = -3/2$ to $\beta_\rho = -4/3$, while the pressure

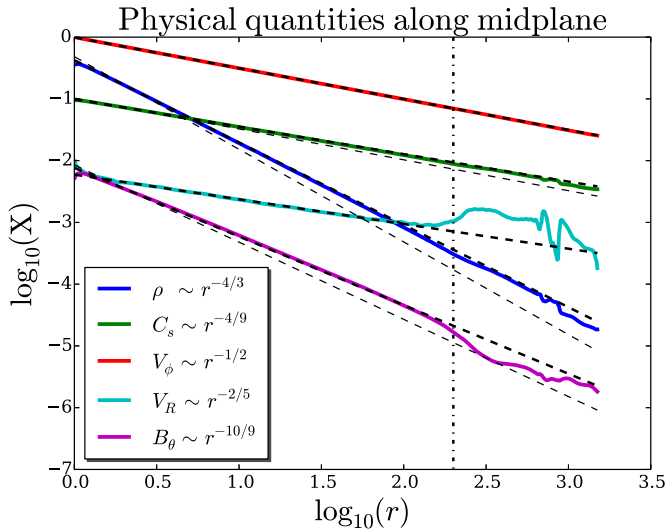


Figure 25. Physical quantities along the midplane for the strong diffusivity model. The colors show different variable profiles, the thick dashed lines correspond to certain power laws, and the mismatched thin dashed lines correspond to the initial distributions of variables. The vertical dashed line marks $r = 200$.

(A color version of this figure is available in the online journal.)

changes from $\beta_p = -5/2$ to $\beta_p = -20/9$. For the accretion velocity, we find a profile of $\beta_{V_R} = -2/5$, and $\beta_{B_\theta} = -10/9$ for the magnetic field. As a consequence, the profile for the magnetization remains about constant $\beta_\mu \sim 2\beta_{B_\theta}/\beta_p = (-20/9)/(20/9)$. The accretion velocity remains subsonic over the whole disk with an accretion Mach number of $V_R/C_s \simeq 0.1$.

Following Ferreira & Pelletier (1995) and considering the mass accretion $\dot{M}_{\text{acc}} \sim R^2 \rho V_R$, it is easy to get the ejection index $\xi = 0.26$. This is in accordance with previous work Sheikhezami et al. (2012).

5.8. Discussion of the New Diffusivity Model

Our strong diffusivity model, Equation (34), does not necessarily lead to a flat magnetization profile. The model does not directly force the magnetization to be uniformly distributed—in contrast, the profile is expected to be outwardly increasing. As we previously showed, the magnetization profile is linked to the ejection index and it has to be positive if the sound speed remains as initially distributed. What we found is that the disk hydrodynamics changes such that the magnetization of the disk remains flat, thus satisfying Equation (33).

Another way of reasoning is the following. In the case of a flat magnetization profile, the result of the simulation is no longer sensitive to the diffusivity model. In other words, it is possible to switch back from the new diffusivity model to the standard model when the radial magnetization profile is uniform (along the midplane). However, the diffusivity parameter α_m has to be correspondingly re-normalized. The only substantial deviation from a uniform profile is in the innermost disk, which might be influenced by the boundary condition. In fact, we performed such a test simulation, switching back from a strong diffusivity to a standard diffusivity model. As expected, the accretion instability begins to manifest itself similarly as before, leading to the typical magnetization profile (increasing toward the center). However, it takes a much longer time to substantially affect the outer parts of the disk.

The steady state solution achieved when using our strong diffusivity model perfectly fits the results obtained by the

standard model (shown previously as a dot in the plots). This actually approves our understanding that the main agent in driving outflows is the actual magnetization, and that the magnetic diffusivity is only the mediator through which the magnetic field structure is being governed. A self-consistent treatment of turbulence is not yet feasible in the context of outflow launching. Therefore, what should be considered first is the resulting magnetic field strength and distribution, but not the diffusivity model itself.

6. CONCLUSIONS

We have presented results of MHD simulations investigating the launching of jets and outflows from a magnetically diffusive accretion disk. The time evolution of the disk structure is self-consistently taken into account. The simulations are performed in axisymmetry applying the MHD code PLUTO 4.0. In contrast to previous work, we have applied a spherical coordinate system and numerical grid, which implies substantial benefits concerning the numerical resolution and the stability (in time evolution) of the simulations.

In particular, we have obtained the following results.

1. Our numerical setup in spherical coordinates for disk–jet-related problems is very robust. The use of spherical geometry in the context of the outflow launching cannot be underestimated. It allows us to study the launching of outflows for a very long time (more than 150,000 time units) on highly resolved (up to 24 cells per disk height) and at the same time very large (1500 r_0) domains. On the other hand, a spherical grid somewhat limits the study of jet propagation, since the resolution far from the origin becomes low. The rather low resolution in the outer disk region, where the dynamical timescales are long, helps to smooth out small-scale disturbances, thus helping to establish a steady state.
2. Our study has approved a robust disk-outflow structure; however, for the highest resolution, the evolution is prone to have some more fluctuations. The ability to evolve the disk for a very long time disentangles the complex interrelations between the essential quantities for the jet launching. Those are the disk actual magnetization (at a certain time and averaged for a certain location), the mass, energy, and angular momentum fluxes, and the jet terminal velocity.
3. Our main result is that it is the actual rather than the initial disk magnetization that plays a key role for the jet formation and directly affects the accretion power. The value of the initial magnetization can fail to properly characterize the disk–jet properties, but sets the overall jet torque and the disk’s magnetic reservoir. This becomes obvious for very weakly magnetized disks ($\mu_0 = 0.003$). In this case, when choosing a low magnetic diffusivity, the magnetic flux can still be accumulated to a high magnetization in the inner disk. We find that the actual magnetization necessary for sustaining a stable jet is of the order of 10^{-3} , in accordance with Murphy et al. (2010).
4. We showed that the ejection Mach number in the case of a moderately strong magnetization ($\mu < 0.15$) is linearly related with respect to the disk magnetization. This is indeed consistent with the linear to the magnetization mass ejection to the accretion relation. The mass ejection index (the ratio between ejection and accretion) is about 0.3 and thus is similar to the literature values.

5. We found that in the case of uniform magnetization, the MHD disk quantities show a self-similar structure, i.e., resulting in approximately the same vertical profile, and a radial power-law distribution. In the case of a strong diffusivity model, we have presented the corresponding power-law indices for all MHD quantities, although we believe that these power-law indices may directly depend on the actual strength of the magnetization. This would be a natural consequence of the ejection index being a function of magnetization as well.
6. We showed that there are two principally different regimes for outflow launching, which are complementary to each other. In the case of weak magnetic fields (below $\mu \approx 0.03$), we see signatures of a strong magnetic shear, which results in less powerful, but more efficient (higher ejection index), outflows. In the case of a higher magnetization, the magnetic shear, the ejection efficiency, and the energy ejection to accretion flux ratio do not strongly depend on magnetization.
7. We found the upper theoretical limit for the parameter specifying the anisotropy χ in the magnetic diffusivity in case of the standard diffusivity model, essentially depending on the actual magnetization in the disk. In the limit of low magnetization, the anisotropy parameter must satisfy $\chi \leq 1/\alpha_m^2$.
8. We showed that in the non-viscous steady state, assuming radial self-similarity, the magnetization profile should be non-decreasing function of radius. In a steady state, jet-launching disks must have a radially increasing profile of the mass accretion rate. This is a requirement of a positive ejection index. Taking into account that (1) the accretion Mach number is proportional to the magnetization and (2) assuming that the radial profile of the sound speed does not strongly deviate from Keplerian, we showed that the index of the magnetization profile is non-negative.

This is paper I in a series of papers that studies the long-term evolution of outflow-generating disks. In two follow up papers, we will present the (1) connection of the jet properties (the potential observables) with the underlying disk quantities, and we will (2) extend the present setup to simulations including a disk magnetic field that is self-generated by a mean-field dynamo.

We thank Andrea Mignone and the PLUTO team for the opportunity to use their code. We appreciate many helpful discussions with Andrea Mignone and also competent suggestions by the anonymous referee. The simulations were performed on the THEO cluster of the Max Planck Institute for Astronomy. This work was partly financed by the SFB 881 of the German science foundation DFG.

APPENDIX A

UNITS AND NORMALIZATION

Here we show the typical normalization to be used to apply our code units to different astrophysical jet-launching objects, such as YSOs and AGNs. The main normalization units are the Keplerian speed at the inner disk radius,

$$V_{K0} = 94 \text{ km s}^{-1} \left(\frac{M}{M_\odot} \right)^{1/2} \left(\frac{R_0}{0.1 \text{ AU}} \right)^{-1/2} \\ = 6.7 \times 10^4 \text{ km s}^{-1} \left(\frac{R_0}{10 R_S} \right)^{-1/2}$$

the time unit that is expressed in units of $T_0 \equiv R_0/V_{K0}$,

$$T_0 = 1.7 \text{ days} \left(\frac{M}{M_\odot} \right)^{-1/2} \left(\frac{R_0}{0.1 \text{ AU}} \right)^{3/2} = 0.5 \text{ days} \left(\frac{R_0}{10 R_S} \right)^{3/2}$$

The mass accretion rate is a parameter which is, in principle, accessible by observation. Thus, the normalization of density ρ_0 can be chosen by setting suitable accretion rates $\dot{M}_0 = R_0^2 \rho_0 V_{K0}$. Assuming $\dot{M}_{\text{acc}} \simeq 10^{-7} M_\odot \text{ yr}^{-1}$, $\dot{M}_{\text{acc}} \simeq 10 M_\odot \text{ yr}^{-1}$, and taking into account that the typical accretion rates our simulations provide are of the order of $\dot{M}_{\text{acc}} \simeq 0.01$ (in code units), one gets

$$\dot{M}_0 = 3 \times 10^{-5} M_\odot \text{ yr}^{-1} \left(\frac{\rho_0}{10^{-10} \frac{\text{g}}{\text{cm}^3}} \right) \left(\frac{M}{M_\odot} \right)^{1/2} \left(\frac{R_0}{0.1 \text{ AU}} \right)^{3/2} \\ = 10 M_\odot \text{ yr}^{-1} \left(\frac{\rho_0}{10^{-12} \frac{\text{g}}{\text{cm}^3}} \right) \left(\frac{M}{10^8 M_\odot} \right)^{1/2} \left(\frac{R_0}{10 R_S} \right)^{3/2}.$$

The torque and power are given in units of $\dot{J}_0 = R_0^3 \rho_0 V_{K0}^2$ and $\dot{E}_0 = R_0^2 \rho_0 V_{K0}^3$ respectively,

$$\dot{J}_0 = 3.0 \times 10^{36} \text{ dyne cm} \left(\frac{\rho_0}{10^{-10} \frac{\text{g}}{\text{cm}^3}} \right) \left(\frac{M}{M_\odot} \right) \left(\frac{R_0}{0.1 \text{ AU}} \right)^2 \\ = 1.2 \times 10^{51} \text{ dyne cm} \left(\frac{\rho_0}{10^{-12} \frac{\text{g}}{\text{cm}^3}} \right) \left(\frac{M}{10^8 M_\odot} \right)^3 \left(\frac{R_0}{10 R_S} \right)^2$$

$$\dot{E}_0 = 1.9 \times 10^{35} \text{ erg s}^{-1} \left(\frac{\rho_0}{10^{-10} \frac{\text{g}}{\text{cm}^3}} \right) \left(\frac{M}{M_\odot} \right)^{3/2} \left(\frac{R_0}{0.1 \text{ AU}} \right)^{1/2} \\ = 2.6 \times 10^{46} \text{ erg s}^{-1} \left(\frac{\rho_0}{10^{-12} \frac{\text{g}}{\text{cm}^3}} \right) \left(\frac{M}{10^8 M_\odot} \right)^2 \left(\frac{R_0}{10 R_S} \right)^{1/2}.$$

The magnetic field is normalized to its values at the midplane, $B_0 = \sqrt{8\pi P_0 \mu}$,

$$B_0 = 15 \text{ G} \left(\frac{\mu}{0.1} \right)^{1/2} \left(\frac{\epsilon}{0.1} \right) \left(\frac{\rho_0}{10^{-10} \frac{\text{g}}{\text{cm}^3}} \right)^{1/2} \\ \times \left(\frac{M}{M_\odot} \right)^{1/2} \left(\frac{R_0}{0.1 \text{ AU}} \right)^{-1/2} \\ = 1 \text{ kG} \left(\frac{\mu}{0.1} \right)^{1/2} \left(\frac{\epsilon}{0.1} \right) \left(\frac{\rho_0}{10^{-12} \frac{\text{g}}{\text{cm}^3}} \right)^{1/2} \\ \times \left(\frac{M}{10^8 M_\odot} \right)^{1/2} \left(\frac{R_0}{10 R_S} \right)^{-1/2}.$$

APPENDIX B

CONTROL VOLUMES AND THE FLUXES IN DISK AND JET

For the fluxes of energy and angular momentum, we keep the same notation as for the mass flux,

$$\dot{J}_{\text{acc,kin}} = -2 \int_{S_1}^{S_R} r \rho V_\phi \mathbf{V}_p \cdot d\mathbf{S}, \quad \dot{J}_{\text{acc,mag}} = 2 \int_{S_1}^{S_R} r B_\phi \mathbf{B}_p \cdot d\mathbf{S}. \quad (\text{B1})$$

We define the jet angular momentum flux $\dot{J}_{\text{jet}} = \dot{J}_{\text{jet,kin}} + \dot{J}_{\text{jet,mag}}$ with

$$\dot{J}_{\text{jet,kin}} = -2 \int_{S_S} r \rho V_\phi \mathbf{V}_p \cdot d\mathbf{S}, \quad \dot{J}_{\text{jet,mag}} = 2 \int_{S_S} r B_\phi \mathbf{B} \cdot d\mathbf{S}. \quad (\text{B2})$$

Similarly, we define the accretion power $\dot{E}_{\text{acc}} = \dot{E}_{\text{acc,mec}} + \dot{E}_{\text{acc,mag}} + \dot{E}_{\text{acc,thm}}$ as the sum of the mechanic, magnetic, and thermal energies,

$$\begin{aligned}\dot{E}_{\text{acc,mec}} &= -2 \int_{S_1}^{S_R} \left(\frac{V^2}{2} + \Phi_g \right) \rho \mathbf{V}_p \cdot d\mathbf{S}, \\ \dot{E}_{\text{acc,mag}} &= -2 \int_{S_1}^{S_R} \mathbf{E} \times \mathbf{B} \cdot d\mathbf{S}, \\ \dot{E}_{\text{acc,thm}} &= -2 \int_{S_1}^{S_R} \frac{\gamma}{\gamma - 1} P \mathbf{V}_p \cdot d\mathbf{S},\end{aligned}\quad (\text{B3})$$

and the jet power $\dot{E}_{\text{jet}} = \dot{E}_{\text{jet,kin}} + \dot{E}_{\text{jet,grv}} + \dot{E}_{\text{jet,mag}} + \dot{E}_{\text{jet,thm}}$ with

$$\begin{aligned}\dot{E}_{\text{jet,kin}} &= -2 \int_{S_S} \frac{V^2}{2} \rho \mathbf{V}_p \cdot d\mathbf{S}, \\ \dot{E}_{\text{jet,grv}} &= -2 \int_{S_S} \Phi_g \rho \mathbf{V}_p \cdot d\mathbf{S},\end{aligned}\quad (\text{B4})$$

$$\begin{aligned}\dot{E}_{\text{jet,mag}} &= -2 \int_{S_S} \mathbf{E} \times \mathbf{B} \cdot d\mathbf{S}, \\ \dot{E}_{\text{jet,thm}} &= -2 \int_{S_S} \frac{\gamma}{\gamma - 1} P \mathbf{V}_p \cdot d\mathbf{S}.\end{aligned}\quad (\text{B5})$$

REFERENCES

- Bai, X.-N., & Stone, J. M. 2013, *ApJ*, **767**, 30
- Balbus, S. A., & Hawley, J. F. 1991, *ApJ*, **376**, 214
- Banerjee, R., Klessen, R. S., & Fendt, C. 2007, *ApJ*, **668**, 1028
- Beckwith, K., Armitage, P. J., & Simon, J. B. 2011, *MNRAS*, **416**, 361
- Blandford, R. D., & Payne, D. G. 1982, *MNRAS*, **199**, 883
- Cabrit, S., Edwards, S., Strom, S. E., & Strom, K. M. 1990, *ApJ*, **354**, 687
- Camenzind, M. 1990, *RvMA*, **3**, 234
- Campbell, C. G. 2009, *MNRAS*, **392**, 271
- Casse, F., & Ferreira, J. 2000, *A&A*, **353**, 1115
- Casse, F., & Keppens, R. 2002, *ApJ*, **581**, 988
- Casse, F., & Keppens, R. 2004, *ApJ*, **601**, 90
- Colella, P., & Woodward, P. R. 1984, *JCoPh*, **54**, 174
- Fendt, C. 2009, *ApJ*, **692**, 346
- Fendt, C., & Camenzind, M. 1996, *A&A*, **313**, 591
- Fendt, C., & Sheikhezami, S. 2013, *ApJ*, **774**, 12
- Ferreira, J. 1997, *A&A*, **319**, 340
- Ferreira, J., & Casse, F. 2013, *MNRAS*, **428**, 307
- Ferreira, J., & Pelletier, G. 1995, *A&A*, **295**, 807
- Fromang, S. 2013, *EAS Publications Series*, **62**, 95
- Gaibler, V., Khochfar, S., Krause, M., & Silk, J. 2012, *MNRAS*, **425**, 438
- Goedbloed, J. P., Beliën, A. J. C., Holst, B. V. D., & Keppens, R. 2004, *PhPI*, **11**, 4332
- Gressel, O. 2010, *MNRAS*, **405**, 41
- Hawley, J. F., Gammie, C. F., & Balbus, S. A. 1995, *ApJ*, **440**, 742
- Johansen, A., & Levin, Y. 2008, *A&A*, **490**, 501
- Keppens, R., Casse, F., & Goedbloed, J. P. 2002, *ApJL*, **569**, L121
- King, A. R., Pringle, J. E., & Livio, M. 2007, *MNRAS*, **376**, 1740
- Königl, A., & Salmeron, R. 2011, in *The Effects of Large-Scale Magnetic Fields on Disk Formation and Evolution*, ed. P. J. V. Garcia (Chicago, IL: Univ. of Chicago Press), 283
- Lesur, G., & Longaretti, P.-Y. 2009, *A&A*, **504**, 309
- Li, Z. 1995, *ApJ*, **444**, 848
- Londrillo, P., & del Zanna, L. 2004, *JCoPh*, **195**, 17
- Lubow, S. H., Papaloizou, J. C. B., & Pringle, J. E. 1994, *MNRAS*, **268**, 1010
- Meliani, Z., Casse, F., & Sauty, C. 2006, *A&A*, **460**, 1
- Mignone, A., Bodo, G., Massaglia, S., et al. 2007, *ApJS*, **170**, 228
- Murphy, G. C., Ferreira, J., & Zanni, C. 2010, *A&A*, **512**, A82
- Ouyed, R., & Pudritz, R. E. 1997, *ApJ*, **482**, 712
- Parkin, E. R., & Bicknell, G. V. 2013, *ApJ*, **763**, 99
- Pelletier, G., & Pudritz, R. E. 1992, *ApJ*, **394**, 117
- Pudritz, R. E., & Norman, C. A. 1983, *ApJ*, **274**, 677
- Pudritz, R. E., Ouyed, R., Fendt, C., & Brandenburg, A. 2007, in *Protostars and Planets V* (Tucson, AZ: Univ. of Arizona Press), 277
- Sauty, C., & Tsinganos, K. 1994, *A&A*, **287**, 893
- Shakura, N. I., & Sunyaev, R. A. 1973, *A&A*, **24**, 337
- Sheikhezami, S., Fendt, C., Porth, O., Vaidya, B., & Ghanbari, J. 2012, *ApJ*, **757**, 65
- Simon, J. B., Beckwith, K., & Armitage, P. J. 2012, *MNRAS*, **422**, 2685
- Stone, J. M., Hawley, J. F., Gammie, C. F., & Balbus, S. A. 1996, *ApJ*, **463**, 656
- Tzeferacos, P., Ferrari, A., Mignone, A., et al. 2009, *MNRAS*, **400**, 820
- Tzeferacos, P., Ferrari, A., Mignone, A., et al. 2013, *MNRAS*, **428**, 3151
- Uchida, Y., & Shibata, K. 1985, *PASJ*, **37**, 515
- Ustyugova, G. V., Koldoba, A. V., Romanova, M. M., Chechetkin, V. M., & Lovelace, R. V. E. 1995, *ApJL*, **439**, L39
- Zanni, C., Ferrari, A., Rosner, R., Bodo, G., & Massaglia, S. 2007, *A&A*, **469**, 811